

Interrogating theoretical models of neural computation with deep inference
Sean R. Bittner¹, Agostina Palmigiano¹, Alex T. Piet^{2,3,4}, Chunyu A. Duan⁵, Carlos D. Brody^{2,3,6},
Kenneth D. Miller¹, and John P. Cunningham⁷.

¹Department of Neuroscience, Columbia University,

²Princeton Neuroscience Institute,

³Princeton University,

⁴Allen Institute for Brain Science,

⁵Institute of Neuroscience, Chinese Academy of Sciences,

⁶Howard Hughes Medical Institute,

⁷Department of Statistics, Columbia University

¹ 1 Abstract

² A cornerstone of theoretical neuroscience is the circuit model: a system of equations that captures
³ a hypothesized neural mechanism. Such models are valuable when they give rise to an experi-
⁴ mentally observed phenomenon – whether behavioral or a pattern of neural activity – and thus
⁵ can offer insights into neural computation. The operation of these mechanistic circuits, like all
⁶ models, critically depends on the choices of model parameters. A key process in circuit modeling
⁷ is then to identify the model parameters consistent with observed phenomena: to solve the inverse
⁸ problem. To solve challenging inverse problems modeling neural datasets, neuroscientists have used
⁹ statistical inference techniques to much success. However, most research in theoretical neuroscience
¹⁰ focuses on how computation emerges in biologically interpretable circuit models, and how the model
¹¹ parameters govern computation; it is not focused on the latent structure of empirical models of
¹² noisy experimental datasets. In this work, we present a novel technique that brings the power
¹³ and versatility of the probabilistic modeling toolkit to theoretical inverse problems. Our method
¹⁴ uses deep neural networks to learn parameter distributions with rich structure that have specific
¹⁵ computational properties in biologically relevant models. This methodology is explained through
¹⁶ a motivational example inferring conductance parameters in an STG subcircuit model. Then, with
¹⁷ RNNs of increasing size, we show that only EPI allows precise control over the behavior of inferred
¹⁸ parameters, and that EPI scales better in parameter dimension than alternative techniques. In the
¹⁹ remainder of this work, we explain novel theoretical insights through the examination of intricate
²⁰ parametric structure in complex circuit models. In a model of primary visual cortex with multiple

21 neuron-types, where analysis becomes untenable with each additional neuron-type, we discovered
22 how noise distributed across neuron-types governs the excitatory population. Finally, in a model
23 of superior colliculus, we identified and characterized two distinct regimes of connectivity that
24 facilitate switching between opposite tasks amidst interleaved trials. We also found that all task-
25 switching connectivities in this model reproduce behaviors from inactivation experiments, further
26 establishing this hypothesized circuit model. Beyond its scientific contribution, this work illustrates
27 the variety of analyses possible once deep learning is harnessed towards solving theoretical inverse
28 problems.

29 2 Introduction

30 The fundamental practice of theoretical neuroscience is to use a mathematical model to understand
31 neural computation, whether that computation enables perception, action, or some intermediate
32 processing. A neural circuit is systematized with a set of equations – the mechanistic model – and
33 these equations are motivated by biophysics, neurophysiology, and other conceptual considerations
34 [1–4]. The function of this system is governed by the choice of model *parameters*, which when
35 configured in a particular way, give rise to a measurable signature of a computation. The work
36 of analyzing a model then requires solving the inverse problem: given a computation of interest,
37 how can we reason about particular parameter configurations? The inverse problem is crucial for
38 reasoning about likely parameter values, uniquenesses and degeneracies, and predictions made by
39 the model [5, 6].

40 Consider the idealized practice: one carefully designs a model and analytically derives how compu-
41 tational properties determine model parameters. Seminal examples of this gold standard include
42 our field’s understanding of memory capacity in associative neural networks [7], chaos and au-
43 tocorrelation timescales in random neural networks [8], the paradoxical effect [9], and decision
44 making [10]. Unfortunately, as circuit models include more biological realism, theory via analytical
45 derivation becomes intractable. Still, we can gain insight into these complex models by identifying
46 the distribution of parameters that produce computations. By solving the inverse problem in this
47 way, scientific analysis of biologically realistic models is made possible [6, 11–14].

48 As models of computation become more complex, two problems arise with existing approaches.
49 First, the level of insight into computation afforded by parameter inference techniques [15–36] (see
50 review, [37]) is limited by the quantity and quality of available data. Even with vast amounts of

51 data recorded with state-of-the-art equipment, neural activity in non-movement generating brain
52 areas have been shown to strongly encode uninstructed behavior [38–40]. Thus, the observational
53 datasets we use to constrain our models of computation represent computations embedded in a
54 sea of task-irrelevant factors like behavioral idiosyncrasies and likely other factors like hunger and
55 thirst state, and abstract internal thoughts. Thus, when examining parameters inferred from neural
56 datasets, rather than the specific computational properties – the *emergent phenomena* – of neural
57 circuit models [7–10], its impossible to identify which aspect of the neural data is determining the
58 inferred parameters: the computation or extraneous factors.

59 Second, most neural circuit models in theoretical neuroscience are noisy systems of differential
60 equations that can only be sampled or realized through forward simulation; they lack a tractable
61 likelihood function, which is necessary for statistical inference. Therefore, the most popular ap-
62 proaches to theoretical inverse problems have been likelihood-free inference methods [41, 42], in
63 which reasonable parameters are obtained via simulation and rejection. A new class of tech-
64 niques [43–45] use deep learning to improve upon traditional likelihood-free inference approaches.
65 However, to use these methods in theoretical neuroscience, we still must represent computation
66 with an explicit dataset in some way. Theorists are therefore barred from using the probabilistic
67 modeling toolkit for science with circuit models, unless they reformulate their inverse problem into
68 a framework for observational datasets.

69 These challenges motivate the development of a novel inference framework called emergent property
70 inference (EPI). As an adaption of variational inference [46], EPI infers parameter distributions
71 that produce an emergent property: not a singular dataset, but a collection of datasets exhibiting
72 some mathematical criteria. EPI constrains the predictions of the inferred parameter distribution
73 to produce the emergent property, which requires a variant of probabilistic inference methods [47].
74 Importantly, EPI uses deep learning to make rich, flexible approximations to the parameter distri-
75 bution [48] that produces an emergent property. The structure captured by these deep probability
76 distributions are scientifically valuable, revealing the sensitivity and robustness of the emergent
77 property to different parameter combinations. Perhaps most powerfully, EPI facilitates inference
78 in mechanistic models, allowing theorists to capture rich parametric structure in biologically real-
79 istic models that is conditioned upon the emergent phenomena of interest.

80 Equipped with this method, we prove out the potential of EPI by demonstrating its capabilities and
81 presenting novel theoretical findings borne from its analysis. First, we show EPI’s ability to handle
82 mechanistic models using a classic model of parametric degeneracy in biology: the stomatogastric

83 ganglion [49, 50]. Then, we show EPI’s scalability to high dimensional parameter distributions by
84 inferring connectivities of recurrent neural networks (RNNs) that exhibit stable, yet amplified re-
85 sponses – a hallmark of neural responses throughout the brain [51–53]. In a model of primary visual
86 cortex (V1) [54, 55] with different neuron-types, we show that the equation for excitatory variabil-
87 ity become analytically intractable as more populations are added. Strikingly, the way in which
88 noisy inputs across neuron-types governs excitatory variability is salient in the visualized structure
89 of the EPI inferred parameter distribution. Finally, we investigated the possible connectivities of
90 superior colliculus (SC) that allow execution of different tasks on interleaved trials [56]. EPI dis-
91 covered a rich distribution containing two connectivity regimes with different solution classes. We
92 queried the deep probability distribution learned by EPI to produce a mechanistic understanding
93 of cortical responses in each regime. Intriguingly, all inferred connectivities reproduced results from
94 optogenetic inactivation experiments in this behavioral paradigm – emergent phenomena that EPI
95 was not conditioned upon. These theoretical insights afforded by EPI illustrate the value of deep
96 inference for the interrogation of neural circuit models.

97 3 Results

98 3.1 Motivating emergent property inference of theoretical models

99 Consideration of the typical workflow of theoretical modeling clarifies the need for emergent prop-
100 erty inference. First, one designs or chooses an existing model that, it is hypothesized, captures
101 the computation of interest. To ground this process in a well-known example, consider the stom-
102 atogastric ganglion (STG) of crustaceans, a small neural circuit which generates multiple rhythmic
103 muscle activation patterns for digestion [57]. Despite full knowledge of STG connectivity and a
104 precise characterization of its rhythmic pattern generation, biophysical models of the STG have
105 complicated relationships between circuit parameters and computation [12, 49]. A subcircuit model
106 of the STG [50] is shown schematically in Figure 1A. The jagged connections indicate electrical cou-
107 pling having electrical conductance g_{el} , smooth connections in the diagram are inhibitory synaptic
108 projections having strength g_{synA} onto the hub neuron, and $g_{synB} = 5\text{nS}$ for mutual inhibitory con-
109 nections. Note that the behavior of this model will be critically dependent on its parameterization
110 – the choices of conductance parameters $\mathbf{z} = [g_{el}, g_{synA}]$. Specifically, the two fast neurons ($f1$ and
111 $f2$) mutually inhibit one another, and oscillate at a faster frequency than the mutually inhibiting
112 slow neurons ($s1$ and $s2$). The hub neuron (hub) couples with either the fast or slow population,

113 or both.

114 Second, once the model is selected, one must specify what the model should produce. In typical
115 statistical inference, this is a dataset – either collected experimentally or constructed by scientists
116 to fit this empirical paradigm. In EPI, a different approach is taken, in which we define an emergent
117 property: a set of mathematical criteria to be obeyed by the datasets predicted by the inferred
118 distribution. In the STG example, we are concerned with neural spiking frequency, which emerges
119 from the dynamics of the circuit model 1B. An interesting emergent property of this stochastic
120 model is when the hub neuron fires at an intermediate frequency between the intrinsic spiking rates
121 of the fast and slow populations. This emergent property is shown in Figure 1C at an average
122 frequency of 0.55Hz.

123 Third, the model parameters producing these outputs are inferred. Most often, brute-force pa-
124 rameter sweeps or rejection sampling techniques [42] are used to identify parameters whose model
125 simulations are close to data or some desired feature. In this last step lies the opportunity for a
126 paradigmatic shift away from empirical data-oriented representations of model output. By precisely
127 quantifying the emergent property of interest as a statistical feature of the model, we can infer a
128 probability distribution over parameter configurations that produce this emergent property. This
129 unlocks the deep probabilistic modeling toolkit for treating theoretical inverse problems.

130 Before presenting technical details (in the following section), let us understand emergent property
131 inference schematically: EPI (Fig. 1D) takes, as input, the model and the specified emergent
132 property, and as its output, produces the parameter distribution EPI (Fig. 1E). This distribution
133 – represented for clarity as samples from the distribution – is a parameter distribution producing
134 the emergent property. In the STG model, this distribution can be specifically queried to reveal
135 the prototypical parameter configuration for intermediate hub frequency (the mode; Figure 1E
136 yellow star), and how it decays based on changes away from the mode. Indeed, samples equidistant
137 from the mode along these EPI-identified dimensions of sensitivity (v_1) and degeneracy (v_2) (Fig.
138 1E, arrows) agree with error contours (Fig. 1E contours) and have diminished or preserved hub
139 frequency, respectively (Fig. 1F activity traces) (see Section 5.2.1).

140 3.2 A deep generative modeling approach to emergent property inference

141 Emergent property inference (EPI) formalizes the three-step procedure of the previous section with
142 deep probability distributions. First, as is typical, we consider the model as a coupled set of differ-



Figure 1: Emergent property inference (EPI) in the stomatogastric ganglion. **A.** Conductance-based biophysical model of the STG subcircuit. **B.** Spiking frequency $\omega(\mathbf{x}; \mathbf{z})$ is an emergent property statistic. Simulated at $g_{el} = 4.5\text{nS}$ and $g_{synA} = 3\text{nS}$. **C.** The emergent property of intermediate hub frequency. Simulated activity traces are colored by $\log q_\theta(\mathbf{z} | \mathcal{X})$ of generating parameters. (Panel E). **D.** For a choice of model and emergent property, emergent property inference (EPI) learns a deep probability distribution of parameters \mathbf{z} . **E.** The EPI distribution producing intermediate hub frequency. Samples are colored by \log probability density. Contours of hub neuron frequency error are shown at levels of $.525, .53, \dots, .575$ Hz (dark to light gray away from mean). Dimension of sensitivity \mathbf{v}_1 (solid) and degeneracy \mathbf{v}_2 . **F (Top)** The predictive distribution of EPI. The black and gray dashed lines show the mean and two standard deviations according the emergent property. (Bottom) Simulations at the starred parameter values.

143 ential equations [50]. In the running STG example, the model activity $\mathbf{x} = [x_{f1}, x_{f2}, x_{\text{hub}}, x_{s1}, x_{s2}]$ is
 144 the membrane potential for each neuron, which evolves according to the biophysical conductance-
 145 based equation:

$$C_m \frac{d\mathbf{x}(t)}{dt} = -h(\mathbf{x}(t); \mathbf{z}) + d\mathbf{B} \quad (1)$$

146 where $C_m = 1\text{nF}$, and \mathbf{h} is a sum of the leak, calcium, potassium, hyperpolarization, electrical, and
 147 synaptic currents, all of which have their own complicated dependence on activity \mathbf{x} and parameters
 148 $\mathbf{z} = [g_{el}, g_{synA}]$, and $d\mathbf{B}$ is white gaussian noise (see Section 5.2.1 for more detail).

149 Second, we define the emergent property, which as above is “intermediate hub frequency” (Figure
 150 1C). Quantifying this phenomenon is straightforward: we stipulate that the hub neuron’s spiking
 151 frequency – denoted $\omega_{\text{hub}}(\mathbf{x})$ is close to a frequency of 0.55Hz. Mathematically, we achieve this
 152 with two constraints: by fixing the mean hub frequency over the inferred parameter distribution of
 153 \mathbf{z} and its resulting simulations \mathbf{x} to 0.55Hz,

$$\mathbb{E}_{\mathbf{z}, \mathbf{x}} [\omega_{\text{hub}}(\mathbf{x}; \mathbf{z})] = [0.55] \quad (2)$$

154 and requiring that the variance of the hub frequency over the produced simulations is small

$$\text{Var}_{\mathbf{z}, \mathbf{x}} [\omega_{\text{hub}}(\mathbf{x}; \mathbf{z})] = [0.025^2]. \quad (3)$$

155 This level of variance was chosen to be low enough to exclude the fast and slow frequencies of
 156 the two populations, but large enough to allow structural examination of the inferred parameter
 157 distribution. By constraining the means and variances of emergent property statistics over \mathbf{z} as
 158 well as the stochasticity of \mathbf{x} , we can precisely control the behavior that the inferred distribution
 159 that EPI infers. In general, an emergent property

$$\mathcal{X}: \mathbb{E}_{\mathbf{z}, \mathbf{x}} [f(\mathbf{x}; \mathbf{z})] = \boldsymbol{\mu}, \text{Var}_{\mathbf{z}, \mathbf{x}} [f(\mathbf{x}; \mathbf{z})] = \boldsymbol{\sigma}^2 \quad (4)$$

160 defines a collection of datasets with a statistic $f(\mathbf{x}; \mathbf{z})$ (which may be comprised of multiple statis-
 161 tics) and the means $\boldsymbol{\mu}$ and variances $\boldsymbol{\sigma}^2$ of those statistics over the datasets. The choice of $\boldsymbol{\sigma}^2$
 162 predicates the degree of variability around the mean $\boldsymbol{\mu}$ that is consistent with the emergent prop-
 163 erty.

164 Third, we perform emergent property inference: we find a distribution over parameter configura-
 165 tions \mathbf{z} , and insist that samples from this distribution produce the emergent property; in other
 166 words, they obey the constraints introduced in Equation 4. This distribution will be chosen from a

family of probability distributions $\mathcal{Q} = \{q_{\theta}(\mathbf{z}) : \theta \in \Theta\}$, defined by a deep neural network [48,58,59] (Figure 1D, EPI box). Deep probability distributions map a simple random variable \mathbf{z}_0 through a deep neural network with weights and biases θ to parameters $\mathbf{z} = g_{\theta}(\mathbf{z}_0)$ to a suitable complicated distribution (see Section 5.1.2 for more details). Many distributions in \mathcal{Q} will respect the emergent property constraints, so we select the most random (or “entropic”) distribution, which is the same choice made in Bayesian inference (see Section 5.1.6). In EPI optimization, stochastic gradient steps in θ are taken such that entropy is maximized, and the emergent property \mathcal{X} is produced (see Section 5.1) The inferred EPI distribution is denoted $q_{\theta}(\mathbf{z} | \mathcal{X})$, to emphasize that we have conditioned our parameter distribution on emergent property \mathcal{X} .

The major scientific value of EPI is in the rich, queryable structure of these deep probability distributions. The probabilities of $q_{\theta}(\mathbf{z} | \mathcal{X})$ are the densities of these parameters in the distribution producing the emergent property. The greatest probabilities (the modes) indicate prototypical parameter configurations, and the manner in which probabilities change away from the modes shows how different parameter combinations preserve or diminish the emergent property. The dimensions of greatest sensitivity (e.g. Fig. 1E solid arrow) or degeneracy (e.g. Fig. 1E dashed arrow) can be measured directly from the second order derivative of $\log q_{\theta}(\mathbf{z} | \mathcal{X})$ called the “Hessian.” Around the mode, eigenvalues of the Hessian are negative; probabilities decrease locally in all directions away from the mode. The eigenvector with most negative eigenvalue is the parameter combination causing probability to decrease the fastest, making it the most sensitive dimension. Likewise, the flattest eigenvector, corresponding to the least negative eigenvalue, points in the most degenerate dimension. Once an EPI distribution has been inferred, this second order derivative requires trivial computation (when correct architecture class is chosen, see Section 5.1.2).

In the following sections, we showcase the versatility of EPI for scientific analysis on three neural circuit models across ranges of biological realism, neural system function, and network scale. First, we demonstrate the superior scalability of EPI compared to alternative techniques by inferring high-dimensional distributions of RNN connectivities that exhibit amplified, yet stable responses. Also in this RNN example, we emphasize that EPI is the only technique that controls the predictions made by the inferred parameter distribution. Next, in a model of primary visual cortex [54, 55], we show how to gain insight by comparing multiple inferred distributions. Finally, we used EPI to capture subtle parametric structure allowing the mechanistic characterization of multiple parametric regimes of superior colliculus activity in a model of task switching [56]. This work is the first to produce this level of theoretical insight via the quantification and examination of the

199 intricate structure captured by deep probability distributions.

200 **3.3 Scaling inference of RNN connectivity with EPI**

201 Transient amplification is a hallmark of neural activity throughout cortex, and is often thought to be
202 intrinsically generated by recurrent connectivity in the responding cortical area [51–53]. It has been
203 shown that to generate such amplified, yet stabilized responses, the connectivity of RNNs must be
204 non-normal [51, 60], and satisfy additional constraints [61]. In theoretical neuroscience, RNNs are
205 optimized and then examined to show how dynamical systems could execute a given computation
206 [62, 63], but such biologically realistic constraints on connectivity are ignored during optimization
207 for practical reasons. In general, access to distributions of connectivity adhering to theoretical
208 criteria like stable amplification, chaotic fluctuations [8], or low tangling [64] would add scientific
209 value and context to existing research with RNNs. Here, we use EPI to learn RNN connectivities
210 producing stable amplification, and demonstrate the superior scalability and efficiency of EPI to
211 alternative approaches.

212 We consider a rank-2 RNN with N neurons having connectivity $W = UV^\top$ and dynamics

$$\tau \dot{\mathbf{x}} = -\mathbf{x} + W\mathbf{x}, \quad (5)$$

213 where $U = [\mathbf{u}_1 \ \mathbf{u}_2] + g\chi^{(U)}$, $V = [\mathbf{v}_1 \ \mathbf{v}_2] + g\chi^{(V)}$, $\mathbf{u}_1, \mathbf{u}_2, \mathbf{v}_1, \mathbf{v}_2 \in [-1, 1]^N$, and $\chi_{i,j}^{(U)}, \chi_{i,j}^{(V)} \sim$
214 $\mathcal{N}(0, 1)$. We infer connectivity parameterizations $\mathbf{z} = [\mathbf{u}_1^\top, \mathbf{u}_2^\top, \mathbf{v}_1^\top, \mathbf{v}_2^\top]^\top$ that produce stable ampli-
215 fication. Two conditions are necessary and sufficient for RNNs to exhibit stable amplification [61]:
216 $\text{real}(\lambda_1) < 1$ and $\lambda_1^s > 1$, where λ_1 is the eigenvalue of W with greatest real part and λ^s is the max-
217 imum eigenvalue of $W^s = \frac{W+W^\top}{2}$. RNNs with $\text{real}(\lambda_1) = 0.5 \pm 0.5$ and $\lambda_1^s = 1.5 \pm 0.5$ will be stable
218 with modest decay rate ($\text{real}(\lambda_1)$ close to its upper bound of 1) and exhibit modest amplification
219 (λ_1^s close to its lower bound of 1). EPI can naturally condition on this emergent property

$$\begin{aligned} \mathcal{X} : \mathbb{E}_{\mathbf{z}, \mathbf{x}} \begin{bmatrix} \text{real}(\lambda_1) \\ \lambda_1^s \end{bmatrix} &= \begin{bmatrix} 0.5 \\ 1.5 \end{bmatrix} \\ \text{Var}_{\mathbf{z}, \mathbf{x}} \begin{bmatrix} \text{real}(\lambda_1) \\ \lambda_1^s \end{bmatrix} &= \begin{bmatrix} 0.25^2 \\ 0.25^2 \end{bmatrix}, \end{aligned} \quad (6)$$

220 under the notion that variance constraints with standard deviation 0.25 predicate that the vast
221 majority of samples (those within two standard deviations) are within the specified ranges.

222 For comparison, we infer the parameters \mathbf{z} likely to produce stable amplification using two alter-
223 native likelihood-free inference approaches. We ran sequential Monte Carlo approximate Bayesian



Figure 2: **A.** Wall time of EPI (blue), SNPE (orange), and SMC-ABC (green) to converge on RNN connectivities producing stable amplification. Each dot shows convergence time for an individual random seed. For reference, the mean wall time for EPI to achieve its full constraint convergence (means and variances) is shown (blue line). **B.** Simulation count of each algorithm to achieve convergence. Same conventions as A. **C.** The predictive distributions of connectivities inferred by EPI (blue), SNPE (orange), and SMC-ABC (green), with reference to $\mathbf{x}_0 = \mu$ (gray star). **D.** Simulations of networks inferred by each method ($\tau = 100ms$). Each trace (15 per algorithm) corresponds to simulation of one z . (Below) Ratio of obtained samples producing stable amplification, monotonic decay, and instability.

computation (SMC-ABC) [41] and sequential neural posterior estimation (SNPE) [43] with observation $\mathbf{x}_0 = \boldsymbol{\mu}$. SMC-ABC is a rejection sampling approach that SMC techniques to improve efficiency, and SNPE approximates posteriors with deep probability distributions using a two-network architecture (see Section 5.1.1). Unlike EPI, these statistical inference techniques do not control the mean or variance of the predictive distribution, and these predictions of the inferred posteriors are typically affected by model characteristics (e.g. N and g , Fig. 11). To compare the efficiency of these different techniques, we measured the time and number of simulations necessary for the distance of the predictive mean to be less than 0.5 from $\boldsymbol{\mu} = \mathbf{x}_0$ (see Section 5.2.2).

As the number of neurons N in the RNN is scaled, and thus the dimension of the parameter space $\mathbf{z} \in [-1, 1]^{4N}$, we see that EPI converges at greater speed and at greater dimension than SMC-ABC and SNPE (Fig. 2A). It also becomes most efficient to use EPI in terms of simulation count at $N = 50$ (Fig. 2B). It is well known that ABC techniques struggle in dimensions greater than about 30 [65], yet we were careful to assess the scalability of the more comparable approach SNPE. Between EPI and SNPE, we closely controlled the number of parameters in deep probability distributions by dimensionality (Fig. 10), and tested more aggressive SNPE hyperparameterizations when SNPE failed to converge (Fig. 12). From this analysis, we see that deep inference techniques EPI and SNPE are far more amenable to inference of high dimensional parameter distributions than rejection sampling techniques like SMC-ABC, and that EPI outperforms SNPE in both criteria in high dimensions.

No matter the number of neurons, EPI always produces connectivity distributions with mean and variance of $\text{real}(\lambda_1)$ and λ_1^s according to \mathcal{X} (Fig. 2C, blue). For the dimensionalities in which SMC-ABC is tractable, the inferred parameters are concentrated and offset from \mathbf{x}_0 (Fig. 2C, green). When using SNPE the predictions of the inferred parameters are highly concentrated at some RNN sizes and widely varied in others (Fig. 2C, orange). We see these properties reflected in simulations from the inferred distributions: EPI produces a consistent variety of stable, amplified activity norms $|r(t)|$, SMC-ABC produces a limited variety of responses, and the changing variety of responses from SNPE emphasizes the control of EPI on parameter predictions.

Through this example, we have shown that EPI can be used for well-controlled insight into RNNs with respect to their theoretical properties. EPI outperforms SNPE in high dimensions by using gradient information (from $\nabla_{\mathbf{z}} f(\mathbf{x}; \mathbf{z}) = \nabla_{\mathbf{z}} [\text{real}(\lambda_1), \lambda_1^s]^{\top}$) on each optimization iteration. This agrees with recent speculation that such gradient information could improve the efficiency of LFI techniques [66]. While scaling to high dimensions is important, we show in the next two sections

256 how insight can be gained by inspecting structure in lower dimensional parameter distributions.

257 **3.4 EPI reveals how noisy input across neuron-types governs excitatory vari-
258 ability in a V1 model**

259 Dynamical models of excitatory (E) and inhibitory (I) populations with supralinear input-output
260 function have succeeded in explaining a host of experimentally documented phenomena. In a regime
261 characterized by inhibitory stabilization of strong recurrent excitation, these models give rise to
262 paradoxical responses [9], selective amplification [51, 60], surround suppression [67] and normaliza-
263 tion [68]. Despite their strong predictive power, E-I circuit models rely on the assumption that
264 inhibition can be studied as an indivisible unit. However, experimental evidence shows that inhibi-
265 tion is composed of distinct elements – parvalbumin (P), somatostatin (S), VIP (V) – composing
266 80% of GABAergic interneurons in V1 [69–71], and that these inhibitory cell types follow specific
267 connectivity patterns (Fig. 3A) [72]. While research has shown that V1 only shares specific dimen-
268 sions of neuronal variability with downstream areas [73], the role played by recurrent dynamics and
269 the connectivity across neuron-type populations is not understood. Here, in a model of V1 with
270 biologically realistic connectivity, we use EPI to show how the structure of input across neuron
271 types affects the variability of the excitatory population – the population largely responsible for
272 projecting to other brain areas [74].

273 We considered response variability of a nonlinear dynamical V1 circuit model (Fig. 3A) with a
274 state comprised of each neuron-type population’s rate $\mathbf{x} = [x_E, x_P, x_S, x_V]^\top$. Each population
275 receives recurrent input $W\mathbf{x}$, where W is the effective connectivity estimated from post-synaptic
276 potential and connectivity rate measurements (see Section 5.2.3). Each population also experiences
277 an external input \mathbf{h} , which determines population rate via supralinear nonlinearity $\phi(\cdot) = [\cdot]_+^2$. To
278 build on previous work, we model visual contrast-dependent input to the E- and P-populations
279 $\mathbf{h} = \mathbf{b} + c\mathbf{h}_c$. There is also an additive noisy input ϵ parameterized by variances for each neuron
280 type population $\mathbf{z} = \boldsymbol{\sigma}^2 = [\sigma_E^2, \sigma_P^2, \sigma_S^2, \sigma_V^2]$. This noise has a slower dynamical timescale $\tau_{\text{noise}} > \tau$
281 then the population rate, allowing fluctuations around a stimulus-dependent steady-state

$$\tau \frac{d\mathbf{x}}{dt} = -\mathbf{x} + \phi(W\mathbf{x} + \mathbf{h} + \epsilon). \quad (7)$$

282 This model is the stochastic stabilized supralinear network (SSSN) [75] generalized to have mul-
283 tiple inhibitory neuron types, and introduces stochasticity to previous four neuron-type models
284 of V1 [54]. Stochasticity and inhibitory multiplicity introduce substantial complexity to mathe-

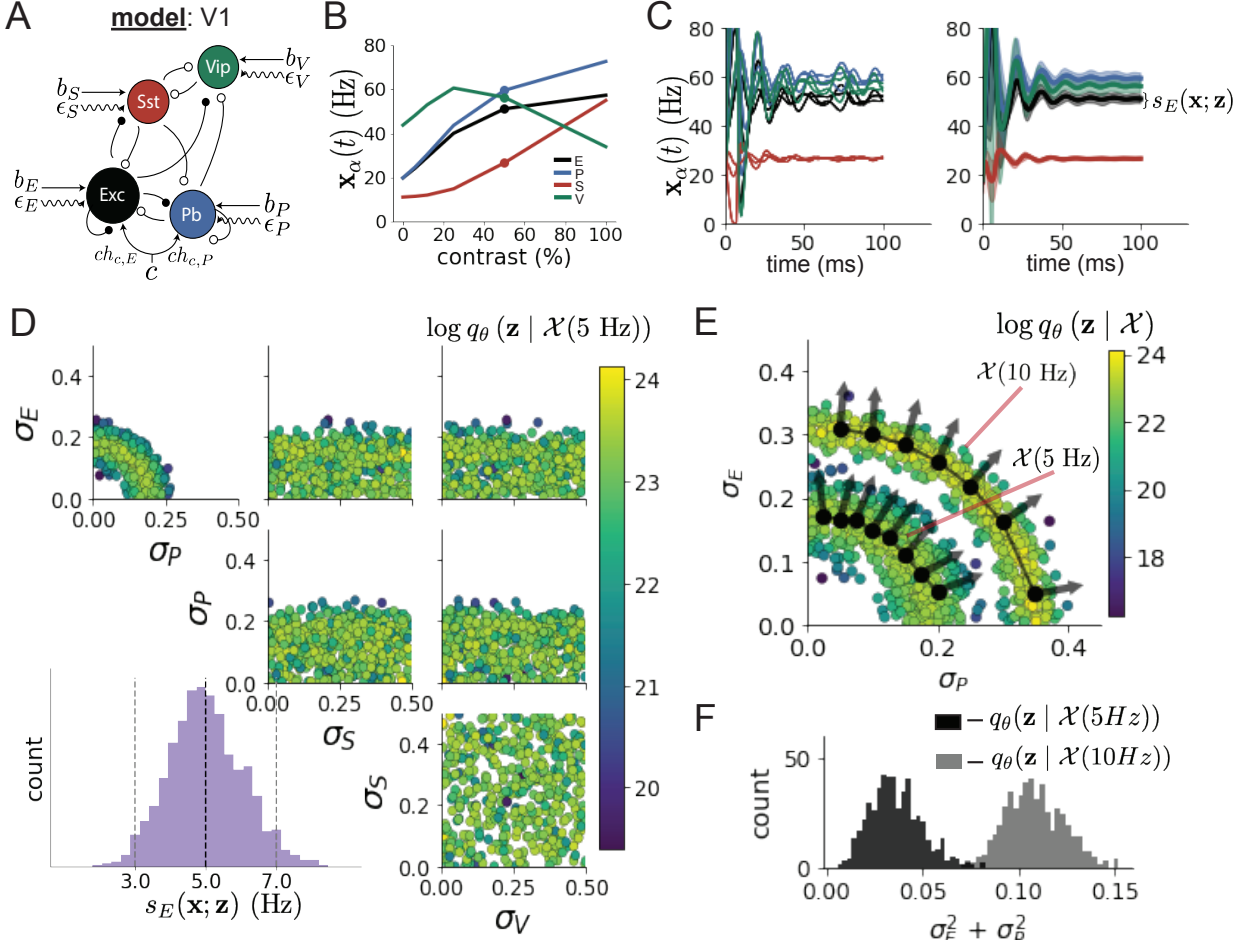


Figure 3: Emergent property inference in the stochastic stabilized supralinear network (SSSN) **A.** Four-population model of primary visual cortex with excitatory (black), parvalbumin (blue), somatostatin (red), and VIP (green) neurons (excitatory and inhibitory projections filled and unfilled, respectively). Some neuron-types largely do not form synaptic projections to others ($|W_{\alpha_1, \alpha_2}| < 0.025$). Each neural population receives a baseline input \mathbf{h}_b , and the E- and P-populations also receive a contrast-dependent input \mathbf{h}_c . Additionally, each neural population receives a slow noisy input ϵ . **B.** Steady-state responses of the SSN model (deterministic, $\sigma = \mathbf{0}$) to varying contrasts. The response at 50% contrast (dots) is the focus of our analysis. **C.** Transient network responses of the SSSN model at 50 % contrast. (Left) Traces are independent trials with varying initialization $\mathbf{x}(0)$ and noise realization. (Right) Mean (solid line) and standard deviation (shading) of responses. **D.** EPI distribution of noise parameters \mathbf{z} conditioned on E-population variability. The EPI predictive distribution of $s_E(\mathbf{x}; \mathbf{z})$ is show on the bottom-left. **E.** (Top) Enlarged visualization of the σ_E - σ_P marginal distribution of EPI $q_\theta(\mathbf{z} | \mathcal{X}(5 \text{ Hz}))$ and $q_\theta(\mathbf{z} | \mathcal{X}(10 \text{ Hz}))$. Each black dot shows the mode at each σ_P . The arrows show the most sensitive dimensions of the Hessian evaluated at these modes. **F.** The predictive distributions of $\sigma_E^2 + \sigma_P^2$ of each parameter distribution $q_\theta(\mathbf{z} | \mathcal{X}(5 \text{ Hz}))$ and $q_\theta(\mathbf{z} | \mathcal{X}(10 \text{ Hz}))$.

285 matical derivations (see Section 5.2.4) motivating the treatment of this model with EPI. Here, we
 286 consider fixed weights W and input \mathbf{h} [55] (Fig. 3B), and study the effect of input variability
 287 $\mathbf{z} = [\sigma_E, \sigma_P, \sigma_S, \sigma_V]^\top$ on excitatory variability at 50% contrast.

288 We quantify different levels y of E-population variability with the emergent property

$$\begin{aligned}\mathcal{X}(y) &: \mathbb{E}_{\mathbf{z}} [s_E(\mathbf{x}; \mathbf{z})] = y \\ \text{Var}_{\mathbf{z}} [s_E(\mathbf{x}; \mathbf{z})] &= 1\text{Hz}^2,\end{aligned}\tag{8}$$

289 where $s_E(\mathbf{x}; \mathbf{z})$ is the standard deviation of the stochastic E -population response about its steady
 290 state (Fig. 3C).

291 We ran EPI to obtain parameter distribution $q_{\theta}(\mathbf{z} | \mathcal{X}(5 \text{ Hz}))$ producing E-population variability
 292 around 5 Hz (Fig. 3D). From the marginal distribution of σ_E and σ_P (Fig. 3D, top-left), we can see
 293 that $s_E(\mathbf{x}; \mathbf{z})$ is sensitive to various combinations of σ_E and σ_P . Alternatively, both σ_S and σ_V are
 294 degenerate with respect to $s_E(\mathbf{x}; \mathbf{z})$ evidenced by the high variability in those dimensions (Fig. 3D,
 295 bottom-right). Together, these observations imply a curved path of parametric degeneracy with
 296 respect to $s_E(\mathbf{x}; \mathbf{z})$ of 5 Hz, which is indicated by the modes along σ_P (Fig. 3E). The dimensions
 297 of sensitivity conferred by EPI and this plain visual structure suggest a quadratic relationship in
 298 the emergent property statistic $s_E(\mathbf{x}; \mathbf{z})$ and parameters \mathbf{z} , which is preserved at a greater level of
 299 variability $\mathcal{X}(10 \text{ Hz})$ (Fig. 3E). Indeed, the sum of squares of σ_E and σ_P is larger in $q_{\theta}(\mathbf{z} | \mathcal{X}(10 \text{ Hz}))$
 300 than $q_{\theta}(\mathbf{z} | \mathcal{X}(5 \text{ Hz}))$ (Fig 3F, $p < 1 \times 10^{-10}$), while the sum of squares of σ_S and σ_V are not
 301 significantly different in the two EPI distributions (Fig. 15, $p = .40$). The strong compensatory
 302 influence of the E- and P-population input variability on excitatory variability is intriguing, since
 303 this circuit exhibited a paradoxical effect in the P-population (and no other inhibitory types) at
 304 50% contrast (Fig. 15) meaning that the E-population is P-stabilized. Future research may uncover
 305 a link between the populations of stabilizations and compensatory interactions governing excitatory
 306 variability.

307 EPI revealed the quadratic relationship between $s_E(\mathbf{x}; \mathbf{z})$ and \mathbf{z} . While this property is ultimately
 308 derivable, we show that with each additional neuron-type population, the formula becomes quite
 309 unruly and likely escapes comprehensible analysis in our case (see Section 5.2.4). This empha-
 310 sizes the need for streamlined methods for gaining understanding about theoretical models when
 311 mathematical analysis becomes prohibitive.

312 **3.5 EPI identifies two regimes of rapid task switching**

313 It has been shown that rats can learn to switch from one behavioral task to the next on randomly
 314 interleaved trials [76], and an important question is what types of neural connectivity allow this
 315 ability. In this experimental setup, rats were explicitly cued on each trial to either orient towards
 316 a visual stimulus in the Pro (P) task or orient away from a visual stimulus in the Anti (A) task
 317 (Fig. 4A). Neural recordings in superior colliculus (SC) exhibited two populations of neurons that
 318 represented task context (Pro or Anti). Furthermore, Pro/Anti neurons in each hemisphere were
 319 strongly correlated with the animal’s decision [56]. These results motivated a model of SC that is
 320 a four-population dynamical system with functionally-defined neuron-types. Here, our goal is to
 321 understand how connectivity in this circuit model governs the ability to switch tasks rapidly.

322 In this SC model, there are Pro- and Anti-populations in each hemisphere (left (L) and right
 323 (R)) with activity variables $\mathbf{x} = [x_{LP}, x_{LA}, x_{RP}, x_{RA}]^\top$. The connectivity of these populations is
 324 parameterized by self sW , vertical vW , diagonal dW and horizontal hW connections (Fig. 4B). The
 325 input \mathbf{h} is comprised of a positive cue-dependent signal to the Pro or Anti populations, a positive
 326 stimulus-dependent input to either the Left or Right populations, and a choice-period input to the
 327 entire network (see Section 5.2.5). Model responses are bounded from 0 to 1 as a function ϕ of an
 328 internal variable \mathbf{u}

$$\begin{aligned}\tau \frac{d\mathbf{u}}{dt} &= -\mathbf{u} + W\mathbf{x} + \mathbf{h} + d\mathbf{B} \\ \mathbf{x} &= \phi(\mathbf{u}).\end{aligned}\tag{9}$$

329 The model responds to the side with greater Pro neuron activation; e.g. the response is left if
 330 $x_{LP} > x_{RP}$ at the end of the trial. Here, we use EPI to determine the network connectivity
 331 $\mathbf{z} = [sW, vW, dW, hW]^\top$ that produces rapid task switching.

332 We define the computation of rapid task switching as accurate execution of each task. Inferred
 333 models should not exhibit fully random responses (50%), or perfect performance (100%), since
 334 perfection is never attained by even the best trained rats. We formulate rapid task switching as an
 335 emergent property by stipulating that the average accuracy in the Pro task $p_P(\mathbf{x}; \mathbf{z})$ and Anti task
 336 $p_A(\mathbf{x}; \mathbf{z})$ be 75% with variance 7.5%².

$$\begin{aligned}\mathcal{X} : \mathbb{E}_{\mathbf{z}} \begin{bmatrix} p_P(\mathbf{x}; \mathbf{z}) \\ p_A(\mathbf{x}; \mathbf{z}) \end{bmatrix} &= \begin{bmatrix} 75\% \\ 75\% \end{bmatrix} \\ \text{Var}_{\mathbf{z}} \begin{bmatrix} p_P(\mathbf{x}; \mathbf{z}) \\ p_A(\mathbf{x}; \mathbf{z}) \end{bmatrix} &= \begin{bmatrix} 7.5\%^2 \\ 7.5\%^2 \end{bmatrix}\end{aligned}\tag{10}$$



Figure 4: **A.** Rapid task switching behavioral paradigm (see text). **B.** Model of superior colliculus (SC). Neurons: LP - left pro, RP - right pro, LA - left anti, RA - right anti. Parameters: sW - self, hW - horizontal, vW - vertical, dW - diagonal weights. **C.** The EPI inferred distribution of rapid task switching networks. Red and purple stars indicate modes \mathbf{z}^* of each connectivity regime. Sensitivity vectors $\mathbf{v}_1(\mathbf{z}^*)$ are shown by arrows. (Bottom-left) EPI predictive distribution of task accuracies. **D.** The connectivity regimes have different responses to perturbation. (Top) Mean and standard error ($N_{\text{test}} = 25$) of accuracy with respect to perturbation along the sensitivity dimension of each mode \mathbf{z}^* . (Middle) Same with perturbation in the dimension of increasing λ_{task} (\mathbf{v}_{task}). (Bottom) Same with perturbation in the dimension of increasing λ_{diag} (\mathbf{v}_{diag}).

337 The EPI inferred distribution (Fig. 4C) produces task accuracies (Fig. 4C, middle-left) according
338 to our mathematical definition of rapid task switching (Equation 10). The patterns of connectivity
339 that govern each task accuracy are nonlinear (Fig. 17A-B); they are not captured well by linear
340 correlations (Fig. 17C). For example, there appear to be two regimes of connectivity: the local
341 structure of the EPI distribution changes dramatically after crossing a threshold of sW (Fig. 17A
342 $sW-hW$ marginal distribution). Not only has EPI captured this intricate, nonlinear distribution,
343 we can use the distribution $q_{\theta}(\mathbf{z} | \mathcal{X})$ returned by EPI to understand these two parametric regimes
344 of SC connectivity.

345 To distinguish these two parts of the distribution, we point out that for many fixed values of
346 parameter hW , there are two modes in the EPI distribution. Thus, by fixing hW to different
347 values and doing gradient ascent on $\log q_{\theta}(\mathbf{z} | \mathcal{X})$ in the parameter spaces proximal to each mode,
348 we can identify a set of modes $\mathbf{z}^*(hW_{\text{fixed}}, r)$ for each putative regime $r \in \{1, 2\}$ (see Section 5.2.5).
349 As hW_{fixed} increases, the modes coalesce to intermediate parameters reflecting a transition between
350 the two sets of modes (Fig. 20 top). However, the sensitivity dimensions of these modes \mathbf{v}_1 (refer
351 to Section 3.2), which reflect the structure of the EPI distribution around each mode, are different
352 across putative regime, yet consistent across hW_{fixed} . This categorical difference in sensitivity
353 dimension across the two sets of modes shows that they indeed represent two different regimes of
354 computation in which connectivity governs computation in different ways.

355 To understand how SC connectivity governs computation in each regime, we can examine how
356 perturbations along $\mathbf{v}_1(\mathbf{z}^*)$ affect task performance in each regime; we measure task accuracy for
357 connectivity changes in the dimension that rapid task switching is most sensitive. While the
358 monotonic increase in Pro accuracy with \mathbf{v}_1 perturbation is largely unaffected by regime (Fig. 4D,
359 top-left), we see a stark difference in Anti accuracy: Anti accuracy falls in either direction of \mathbf{v}_1
360 in regime 1, yet monotonically increases along with Pro accuracy in regime 2 (Fig. 4D, top-right).
361 These two rapid task switching pathologies are caused by distinct connectivity changes ($\mathbf{v}_1(\mathbf{z}^*(\cdot, 1))$
362 vs $\mathbf{v}_1(\mathbf{z}^*(\cdot, 2))$) and explain the sharp change in local structure of the EPI distribution.

363 To understand the connectivity mechanisms that distinguish these two regimes, we perturb connec-
364 tivity at each mode in dimensions that have well defined roles in processing for the Pro and Anti
365 tasks. A convenient property of this connectivity parameterization is that there are \mathbf{z} -invariant
366 eigenmodes of connectivity, whose eigenvalues (or degree of amplification) change with \mathbf{z} . These
367 eigenmodes have intuitive roles in processing in each task, and are accordingly named the *all*,
368 *side*, *task*, and *diag* eigenmodes (see Section 5.2.5). Furthermore, the parameter dimension \mathbf{v}_a

369 ($a \in \{\text{all, side, task, and diag}\}$) that increases the eigenvalue of connectivity λ_a is \mathbf{z} -invariant (un-
370 like the sensitivity dimension $\mathbf{v}_1(\mathbf{z})$) and $\mathbf{v}_a \perp \mathbf{v}_{b \neq a}$. Thus, by changing the degree of amplification
371 of each processing mode by perturbing \mathbf{z} along \mathbf{v}_a , we can elicit the differentiating properties of
372 the two regimes.

373 Through these connectivity perturbation analyses, we found that increasing λ_{task} strongly reduced
374 Pro accuracy in regime 1, yet strongly reduced Anti accuracy in regime 2. This suggests that
375 stronger task representations can inhibit both Pro and Anti task performance in different contexts.
376 Furthermore, changing λ_{task} in either direction decreases Anti performance in regime 1, showing
377 that Anti task performance in regime 1 is dependent on a specific level of task representation.
378 We also found that with increasing λ_{diag} , Pro accuracy increased in both regimes, but there were
379 opposite effects on Anti accuracy. In regime 1, stronger amplification of diagonal population pat-
380 terns decreased Anti accuracy, while in regime 2 accuracy increased. These findings give us an
381 understanding of the mechanistic differences in computation enabling rapid task switching in each
382 regime.

383 **3.6 EPI inferred SC connectivities reproduce results from optogenetic inacti-
384 vation experiments**

385 During the delay period of this task, the circuit must prepare to execute the correct task based on
386 the cue input. Experimental results from Duan et al. found that optogenetic inactivation of SC
387 during the delay period consistently decreased performance in the Anti task, but had no effect on
388 the Pro task (Fig. 5A). All network connectivities inferred by EPI exhibited this same effect, when
389 network activities were silenced during the delay period (see Section 5.2.5). Notably, EPI inferred
390 connectivities were only conditioned upon the emergent property of rapid task switching, not on
391 Anti task failure during delay period silencing.

392 Similarities across Pro and Anti trials in choice period responses following delay period inactivation
393 (Fig. 21A) suggested that connectivity patterns inducing greater Pro task accuracy increase error
394 in delay period inactivated Anti trials (Fig. 5B). The strong anticorrelation between p_P and $p_{A,\text{opto}}$
395 across EPI inferred connectivities led to the following hypothesis about each connectivity regime:
396 the sensitivity dimension of each regime decreases $p_{A,\text{opto}}$ irrespective of its effect on p_A , since
397 both \mathbf{v}_1 and \mathbf{v}_2 increase p_P . Indeed, in regimes 1 and 2 where sensitivity dimensions elicit different
398 responses in p_A , $p_{A,\text{opto}}$ decreases since the connectivity changes enhancing p_P exacerbate Anti trial
399 error (Fig. 5C). Thus, the altered state caused by delay period silencing makes the connectivity

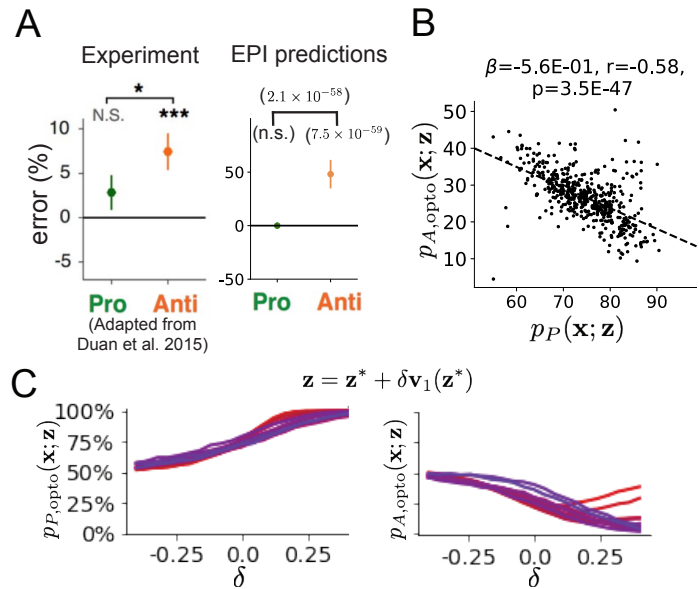


Figure 5: **A.** The EPI distribution predicts experimental results (left) showing no change in the Pro task, but larger error in the Anti task (right). **B.** Accuracy in the Anti task during delay period optogenetic inactivation $p_{A,\text{opto}}$ is strongly anticorrelated with accuracy in the Pro task. **C.** Mean and standard error ($N_{\text{test}} = 25$) of accuracy with respect to perturbation along the sensitivity dimension of each mode \mathbf{z}^* .

400 governing p_P more influential on Anti accuracy than the connectivity governing p_A .
 401 In summary, we used EPI to obtain the full distribution of connectivities that execute rapid task
 402 switching. This EPI distribution revealed two regimes of rapid task switching, which we char-
 403 acterized using the probabilistic toolkit EPI seemlessly affords. We found that both of these
 404 parametric regimes identified by EPI reproduce results from optogenetic inactivation experiments:
 405 when activity is silenced during the delay period, only Anti accuracy suffers. We then identified
 406 the connectivity mechanisms governing Anti accuracy during delay period silencing, and showed
 407 that they are regime invariant.

408 4 Discussion

409 In neuroscience, machine learning has primarily been used to reveal structure in neural datasets [37].
 410 Careful inference procedures are developed for these statistical models allowing precise, quantitative
 411 reasoning, which clarifies the way data informs beliefs about the model parameters. However,
 412 these statistical models often lack resemblance to the underlying biology, making it unclear how
 413 to go from the structure revealed by these methods, to the neural mechanisms giving rise to

414 it. In contrast, theoretical neuroscience has focused on careful mechanistic modeling and the
415 production of emergent properties of computation, rather than measuring structure in some noisy
416 observed dataset. The careful steps of *i.*) model design and *ii.*) emergent property definition,
417 are followed by *iii.*) practical inference methods resulting in an opaque characterization of the
418 way model parameters govern computation. In this work, we improve upon parameter inference
419 techniques in theoretical neuroscience with emergent property inference, harnessing deep learning
420 towards parameter inference with respect to emergent phenomena in interpretable models of neural
421 computation (see Section 5.1.1).

422 Methodology for statistical inference in mechanistic models of neural circuits has evolved consider-
423 ably in recent years. Early work used rejection sampling techniques [41, 77, 78], but more recently
424 developed methodology employs deep learning to improve efficiency or provide flexible distribution
425 approximations. SNPE [43] and other sequential techniques for inference in mechanistic models
426 developed along with EPI (see Section 5.1.1) have been used for posterior inference with noisy
427 experimental datasets. On the other hand, EPI is a deep inference technique designed to condition
428 upon mathematical criteria, such that the parameter distribution only produces the specified *emer-*
429 *gent properties* of computation. EPI is thus ideally suited for questions in theoretical neuroscience,
430 and we show that it has superior scaling properties to these other inference techniques (see Section
431 3.3).

432 In this work, we prove out the utility of deep probability distributions for theoretical neuroscience.
433 While previous work has used SNPE to obtain flexible posterior approximations in mechanistic
434 models conditioned on experimental datasets, we use the rich structure captured by deep probability
435 distributions in EPI to gain new theoretical insights. This is first done in a complex model of V1,
436 where we combine the modeling advancements [54, 75], which make analytic characterization of
437 excitatory variability very complicated. There, EPI clearly and simply revealed the parametric
438 structure of input variability across neuron-type populations that governed excitatory variability,
439 which has implications on the dimensionality and nature information transmission in visual cortex.

440 Finally, we used EPI to identify two distinct regimes of SC connectivity that enabled rapid task
441 switching. By systematically characterizing the local structure of the inferred distribution using the
442 analytic capabilities deep probability distributions, we discerned a mechanistic understanding of
443 each computational regime. Each of these regimes reproduced effects from optogenetic experiments
444 [76], suggesting that both are biologically plausible. These analyses of the V1 and SC models serve
445 as examples of how to leverage the probabilistic toolkit for theoretical insight into models of neural

446 computation.

447 **Acknowledgements:**

448 This work was funded by NSF Graduate Research Fellowship, DGE-1644869, McKnight Endow-
449 ment Fund, NIH NINDS 5R01NS100066, Simons Foundation 542963, NSF NeuroNex Award, DBI-
450 1707398, The Gatsby Charitable Foundation, Simons Collaboration on the Global Brain Postdoc-
451 toral Fellowship, Chinese Postdoctoral Science Foundation, and International Exchange Program
452 Fellowship. Helpful conversations were had with Francesca Mastrogiuseppe, Srdjan Ostojic, James
453 Fitzgerald, Stephen Baccus, Dhruva Raman, Liam Paninski, and Larry Abbott.

454 **Data availability statement:**

455 The datasets generated during and/or analyzed during the current study are available from the
456 corresponding author upon reasonable request.

457 **Code availability statement:**

458 All software written for the current study is available at <https://github.com/cunningham-lab/epi>.

459 **References**

- 460 [1] Nancy Kopell and G Bard Ermentrout. Coupled oscillators and the design of central pattern
461 generators. *Mathematical biosciences*, 90(1-2):87–109, 1988.
- 462 [2] Eve Marder. From biophysics to models of network function. *Annual review of neuroscience*,
463 21(1):25–45, 1998.
- 464 [3] Larry F Abbott. Theoretical neuroscience rising. *Neuron*, 60(3):489–495, 2008.
- 465 [4] Xiao-Jing Wang. Neurophysiological and computational principles of cortical rhythms in
466 cognition. *Physiological reviews*, 90(3):1195–1268, 2010.
- 467 [5] Ryan N Gutenkunst, Joshua J Waterfall, Fergal P Casey, Kevin S Brown, Christopher R
468 Myers, and James P Sethna. Universally sloppy parameter sensitivities in systems biology
469 models. *PLoS Comput Biol*, 3(10):e189, 2007.
- 470 [6] Timothy O’Leary, Alex H Williams, Alessio Franci, and Eve Marder. Cell types, network
471 homeostasis, and pathological compensation from a biologically plausible ion channel expres-
472 sion model. *Neuron*, 82(4):809–821, 2014.

- 473 [7] John J Hopfield. Neural networks and physical systems with emergent collective computa-
474 tional abilities. *Proceedings of the national academy of sciences*, 79(8):2554–2558, 1982.
- 475 [8] Haim Sompolinsky, Andrea Crisanti, and Hans-Jurgen Sommers. Chaos in random neural
476 networks. *Physical review letters*, 61(3):259, 1988.
- 477 [9] Misha V Tsodyks, William E Skaggs, Terrence J Sejnowski, and Bruce L McNaughton. Para-
478 doxical effects of external modulation of inhibitory interneurons. *Journal of neuroscience*,
479 17(11):4382–4388, 1997.
- 480 [10] Kong-Fatt Wong and Xiao-Jing Wang. A recurrent network mechanism of time integration
481 in perceptual decisions. *Journal of Neuroscience*, 26(4):1314–1328, 2006.
- 482 [11] WR Foster, LH Ungar, and JS Schwaber. Significance of conductances in hodgkin-huxley
483 models. *Journal of neurophysiology*, 70(6):2502–2518, 1993.
- 484 [12] Astrid A Prinz, Dirk Bucher, and Eve Marder. Similar network activity from disparate circuit
485 parameters. *Nature neuroscience*, 7(12):1345–1352, 2004.
- 486 [13] Pablo Achard and Erik De Schutter. Complex parameter landscape for a complex neuron
487 model. *PLoS computational biology*, 2(7):e94, 2006.
- 488 [14] Leandro M Alonso and Eve Marder. Visualization of currents in neural models with similar
489 behavior and different conductance densities. *Elife*, 8:e42722, 2019.
- 490 [15] Robert E Kass and Valérie Ventura. A spike-train probability model. *Neural computation*,
491 13(8):1713–1720, 2001.
- 492 [16] Emery N Brown, Loren M Frank, Dengda Tang, Michael C Quirk, and Matthew A Wilson.
493 A statistical paradigm for neural spike train decoding applied to position prediction from
494 ensemble firing patterns of rat hippocampal place cells. *Journal of Neuroscience*, 18(18):7411–
495 7425, 1998.
- 496 [17] Liam Paninski. Maximum likelihood estimation of cascade point-process neural encoding
497 models. *Network: Computation in Neural Systems*, 15(4):243–262, 2004.
- 498 [18] Wilson Truccolo, Uri T Eden, Matthew R Fellows, John P Donoghue, and Emery N Brown.
499 A point process framework for relating neural spiking activity to spiking history, neural
500 ensemble, and extrinsic covariate effects. *Journal of neurophysiology*, 93(2):1074–1089, 2005.

- 501 [19] Elad Schneidman, Michael J Berry, Ronen Segev, and William Bialek. Weak pairwise correlations imply strongly correlated network states in a neural population. *Nature*, 440(7087):1007–1012, 2006.
- 504 [20] Shaul Druckmann, Yoav Banitt, Albert A Gidon, Felix Schürmann, Henry Markram, and Idan Segev. A novel multiple objective optimization framework for constraining conductance-based neuron models by experimental data. *Frontiers in neuroscience*, 1:1, 2007.
- 507 [21] Richard Turner and Maneesh Sahani. A maximum-likelihood interpretation for slow feature analysis. *Neural computation*, 19(4):1022–1038, 2007.
- 509 [22] M Yu Byron, John P Cunningham, Gopal Santhanam, Stephen I Ryu, Krishna V Shenoy, and Maneesh Sahani. Gaussian-process factor analysis for low-dimensional single-trial analysis of neural population activity. In *Advances in neural information processing systems*, pages 510 1881–1888, 2009.
- 513 [23] Jakob H Macke, Lars Buesing, John P Cunningham, Byron M Yu, Krishna V Shenoy, and Maneesh Sahani. Empirical models of spiking in neural populations. *Advances in neural 514 information processing systems*, 24:1350–1358, 2011.
- 516 [24] Il Memming Park and Jonathan W Pillow. Bayesian spike-triggered covariance analysis. In 517 *Advances in neural information processing systems*, pages 1692–1700, 2011.
- 518 [25] Einat Granot-Atedgi, Gašper Tkačik, Ronen Segev, and Elad Schneidman. Stimulus- 519 dependent maximum entropy models of neural population codes. *PLoS Comput Biol*, 520 9(3):e1002922, 2013.
- 521 [26] Kenneth W Latimer, Jacob L Yates, Miriam LR Meister, Alexander C Huk, and Jonathan W 522 Pillow. Single-trial spike trains in parietal cortex reveal discrete steps during decision-making. 523 *Science*, 349(6244):184–187, 2015.
- 524 [27] Kaushik J Lakshminarasimhan, Marina Petsalis, Hyeshin Park, Gregory C DeAngelis, Xaq 525 Pitkow, and Dora E Angelaki. A dynamic bayesian observer model reveals origins of bias in 526 visual path integration. *Neuron*, 99(1):194–206, 2018.
- 527 [28] Lea Duncker, Gergo Bohner, Julien Boussard, and Maneesh Sahani. Learning interpretable 528 continuous-time models of latent stochastic dynamical systems. *Proceedings of the 36th International Conference on Machine Learning*, 2019.

- 530 [29] Josef Ladenbauer, Sam McKenzie, Daniel Fine English, Olivier Hagens, and Srdjan Ostojic.
531 Inferring and validating mechanistic models of neural microcircuits based on spike-train data.
532 *Nature Communications*, 10(4933), 2019.
- 533 [30] Yuanjun Gao, Evan W Archer, Liam Paninski, and John P Cunningham. Linear dynamical
534 neural population models through nonlinear embeddings. In *Advances in neural information*
535 *processing systems*, pages 163–171, 2016.
- 536 [31] Yuan Zhao and Il Memming Park. Recursive variational bayesian dual estimation for non-
537 linear dynamics and non-gaussian observations. *stat*, 1050:27, 2017.
- 538 [32] Gabriel Barello, Adam Charles, and Jonathan Pillow. Sparse-coding variational auto-
539 encoders. *bioRxiv*, page 399246, 2018.
- 540 [33] Chethan Pandarinath, Daniel J O’Shea, Jasmine Collins, Rafal Jozefowicz, Sergey D Stavisky,
541 Jonathan C Kao, Eric M Trautmann, Matthew T Kaufman, Stephen I Ryu, Leigh R
542 Hochberg, et al. Inferring single-trial neural population dynamics using sequential auto-
543 encoders. *Nature methods*, page 1, 2018.
- 544 [34] Alexander B Wiltschko, Matthew J Johnson, Giuliano Iurilli, Ralph E Peterson, Jesse M
545 Katon, Stan L Pashkovski, Victoria E Abraira, Ryan P Adams, and Sandeep Robert Datta.
546 Mapping sub-second structure in mouse behavior. *Neuron*, 88(6):1121–1135, 2015.
- 547 [35] Matthew J Johnson, David K Duvenaud, Alex Wiltschko, Ryan P Adams, and Sandeep R
548 Datta. Composing graphical models with neural networks for structured representations and
549 fast inference. In *Advances in neural information processing systems*, pages 2946–2954, 2016.
- 550 [36] Eleanor Batty, Matthew Whiteway, Shreya Saxena, Dan Biderman, Taiga Abe, Simon Musall,
551 Winthrop Gillis, Jeffrey Markowitz, Anne Churchland, John Cunningham, et al. Behavenet:
552 nonlinear embedding and bayesian neural decoding of behavioral videos. *Advances in Neural*
553 *Information Processing Systems*, 2019.
- 554 [37] Liam Paninski and John P Cunningham. Neural data science: accelerating the experiment-
555 analysis-theory cycle in large-scale neuroscience. *Current opinion in neurobiology*, 50:232–241,
556 2018.
- 557 [38] Cristopher M Niell and Michael P Stryker. Modulation of visual responses by behavioral
558 state in mouse visual cortex. *Neuron*, 65(4):472–479, 2010.

- 559 [39] Aman B Saleem, Ashi Ayaz, Kathryn J Jeffery, Kenneth D Harris, and Matteo Carandini.
560 Integration of visual motion and locomotion in mouse visual cortex. *Nature neuroscience*,
561 16(12):1864–1869, 2013.
- 562 [40] Simon Musall, Matthew T Kaufman, Ashley L Juavinett, Steven Gluf, and Anne K Church-
563 land. Single-trial neural dynamics are dominated by richly varied movements. *Nature neuro-
564 science*, 22(10):1677–1686, 2019.
- 565 [41] Scott A Sisson, Yanan Fan, and Mark M Tanaka. Sequential monte carlo without likelihoods.
566 *Proceedings of the National Academy of Sciences*, 104(6):1760–1765, 2007.
- 567 [42] Juliane Liepe, Paul Kirk, Sarah Filippi, Tina Toni, Chris P Barnes, and Michael PH Stumpf.
568 A framework for parameter estimation and model selection from experimental data in systems
569 biology using approximate bayesian computation. *Nature protocols*, 9(2):439–456, 2014.
- 570 [43] Pedro J Gonçalves, Jan-Matthis Lueckmann, Michael Deistler, Marcel Nonnenmacher, Kaan
571 Öcal, Giacomo Bassetto, Chaitanya Chintaluri, William F Podlaski, Sara A Haddad, Tim P
572 Vogels, et al. Training deep neural density estimators to identify mechanistic models of neural
573 dynamics. *bioRxiv*, page 838383, 2019.
- 574 [44] George Papamakarios, David Sterratt, and Iain Murray. Sequential neural likelihood: Fast
575 likelihood-free inference with autoregressive flows. In *The 22nd International Conference on
576 Artificial Intelligence and Statistics*, pages 837–848. PMLR, 2019.
- 577 [45] Joeri Hermans, Volodimir Begy, and Gilles Louppe. Likelihood-free mcmc with amortized
578 approximate ratio estimators. In *International Conference on Machine Learning*, pages 4239–
579 4248. PMLR, 2020.
- 580 [46] Lawrence Saul and Michael Jordan. A mean field learning algorithm for unsupervised neural
581 networks. In *Learning in graphical models*, pages 541–554. Springer, 1998.
- 582 [47] Gabriel Loaiza-Ganem, Yuanjun Gao, and John P Cunningham. Maximum entropy flow
583 networks. *International Conference on Learning Representations*, 2017.
- 584 [48] Danilo Jimenez Rezende and Shakir Mohamed. Variational inference with normalizing flows.
585 *International Conference on Machine Learning*, 2015.

- 586 [49] Mark S Goldman, Jorge Golowasch, Eve Marder, and LF Abbott. Global structure, ro-
587 bustness, and modulation of neuronal models. *Journal of Neuroscience*, 21(14):5229–5238,
588 2001.
- 589 [50] Gabrielle J Gutierrez, Timothy O’Leary, and Eve Marder. Multiple mechanisms switch an
590 electrically coupled, synaptically inhibited neuron between competing rhythmic oscillators.
591 *Neuron*, 77(5):845–858, 2013.
- 592 [51] Brendan K Murphy and Kenneth D Miller. Balanced amplification: a new mechanism of
593 selective amplification of neural activity patterns. *Neuron*, 61(4):635–648, 2009.
- 594 [52] Guillaume Hennequin, Tim P Vogels, and Wulfram Gerstner. Optimal control of transient dy-
595 namics in balanced networks supports generation of complex movements. *Neuron*, 82(6):1394–
596 1406, 2014.
- 597 [53] Giulio Bondanelli, Thomas Deneux, Brice Bathellier, and Srdjan Ostojic. Population coding
598 and network dynamics during off responses in auditory cortex. *BioRxiv*, page 810655, 2019.
- 599 [54] Ashok Litwin-Kumar, Robert Rosenbaum, and Brent Doiron. Inhibitory stabilization and
600 visual coding in cortical circuits with multiple interneuron subtypes. *Journal of neurophysi-
601 ology*, 115(3):1399–1409, 2016.
- 602 [55] Agostina Palmigiano, Francesco Fumarola, Daniel P Mossing, Nataliya Kraynyukova, Hillel
603 Adesnik, and Kenneth Miller. Structure and variability of optogenetic responses identify the
604 operating regime of cortex. *bioRxiv*, 2020.
- 605 [56] Chunyu A Duan, Marino Pagan, Alex T Piet, Charles D Kopec, Athena Akrami, Alexander J
606 Riordan, Jeffrey C Erlich, and Carlos D Brody. Collicular circuits for flexible sensorimotor
607 routing. *bioRxiv*, page 245613, 2018.
- 608 [57] Eve Marder and Vatsala Thirumalai. Cellular, synaptic and network effects of neuromodula-
609 tion. *Neural Networks*, 15(4-6):479–493, 2002.
- 610 [58] Laurent Dinh, Jascha Sohl-Dickstein, and Samy Bengio. Density estimation using real nvp.
611 *Proceedings of the 5th International Conference on Learning Representations*, 2017.
- 612 [59] George Papamakarios, Theo Pavlakou, and Iain Murray. Masked autoregressive flow for
613 density estimation. In *Advances in Neural Information Processing Systems*, pages 2338–2347,
614 2017.

- 615 [60] Mark S Goldman. Memory without feedback in a neural network. *Neuron*, 61(4):621–634,
616 2009.
- 617 [61] Giulio Bondanelli and Srdjan Ostojic. Coding with transient trajectories in recurrent neural
618 networks. *PLoS computational biology*, 16(2):e1007655, 2020.
- 619 [62] David Sussillo. Neural circuits as computational dynamical systems. *Current opinion in*
620 *neurobiology*, 25:156–163, 2014.
- 621 [63] Omri Barak. Recurrent neural networks as versatile tools of neuroscience research. *Current*
622 *opinion in neurobiology*, 46:1–6, 2017.
- 623 [64] Abigail A Russo, Sean R Bittner, Sean M Perkins, Jeffrey S Seely, Brian M London, Antonio H
624 Lara, Andrew Miri, Najja J Marshall, Adam Kohn, Thomas M Jessell, et al. Motor cortex
625 embeds muscle-like commands in an untangled population response. *Neuron*, 97(4):953–966,
626 2018.
- 627 [65] Scott A Sisson, Yanan Fan, and Mark Beaumont. *Handbook of approximate Bayesian com-*
628 *putation*. CRC Press, 2018.
- 629 [66] Kyle Cranmer, Johann Brehmer, and Gilles Louppe. The frontier of simulation-based infer-
630 ence. *Proceedings of the National Academy of Sciences*, 2020.
- 631 [67] Hirofumi Ozeki, Ian M Finn, Evan S Schaffer, Kenneth D Miller, and David Ferster. Inhibitory
632 stabilization of the cortical network underlies visual surround suppression. *Neuron*, 62(4):578–
633 592, 2009.
- 634 [68] Daniel B Rubin, Stephen D Van Hooser, and Kenneth D Miller. The stabilized supralin-
635 ear network: a unifying circuit motif underlying multi-input integration in sensory cortex.
636 *Neuron*, 85(2):402–417, 2015.
- 637 [69] Henry Markram, Maria Toledo-Rodriguez, Yun Wang, Anirudh Gupta, Gilad Silberberg, and
638 Caizhi Wu. Interneurons of the neocortical inhibitory system. *Nature reviews neuroscience*,
639 5(10):793, 2004.
- 640 [70] Bernardo Rudy, Gordon Fishell, SooHyun Lee, and Jens Hjerling-Leffler. Three groups of
641 interneurons account for nearly 100% of neocortical gabaergic neurons. *Developmental neu-*
642 *robiology*, 71(1):45–61, 2011.

- 643 [71] Robin Tremblay, Soohyun Lee, and Bernardo Rudy. GABAergic Interneurons in the Neocor-
644 tex: From Cellular Properties to Circuits. *Neuron*, 91(2):260–292, 2016.
- 645 [72] Carsten K Pfeffer, Mingshan Xue, Miao He, Z Josh Huang, and Massimo Scanziani. Inhi-
646 bition of inhibition in visual cortex: the logic of connections between molecularly distinct
647 interneurons. *Nature Neuroscience*, 16(8):1068, 2013.
- 648 [73] João D Semedo, Amin Zandvakili, Christian K Machens, M Yu Byron, and Adam Kohn.
649 Cortical areas interact through a communication subspace. *Neuron*, 102(1):249–259, 2019.
- 650 [74] Daniel J Felleman and David C Van Essen. Distributed hierarchical processing in the primate
651 cerebral cortex. *Cerebral cortex (New York, NY: 1991)*, 1(1):1–47, 1991.
- 652 [75] Guillaume Hennequin, Yashar Ahmadian, Daniel B Rubin, Máté Lengyel, and Kenneth D
653 Miller. The dynamical regime of sensory cortex: stable dynamics around a single stimulus-
654 tuned attractor account for patterns of noise variability. *Neuron*, 98(4):846–860, 2018.
- 655 [76] Chunyu A Duan, Jeffrey C Erlich, and Carlos D Brody. Requirement of prefrontal and
656 midbrain regions for rapid executive control of behavior in the rat. *Neuron*, 86(6):1491–1503,
657 2015.
- 658 [77] Mark A Beaumont, Wenyang Zhang, and David J Balding. Approximate bayesian computa-
659 tion in population genetics. *Genetics*, 162(4):2025–2035, 2002.
- 660 [78] Paul Marjoram, John Molitor, Vincent Plagnol, and Simon Tavaré. Markov chain monte carlo
661 without likelihoods. *Proceedings of the National Academy of Sciences*, 100(26):15324–15328,
662 2003.
- 663 [79] Nicholas Metropolis, Arianna W Rosenbluth, Marshall N Rosenbluth, Augusta H Teller, and
664 Edward Teller. Equation of state calculations by fast computing machines. *The journal of
665 chemical physics*, 21(6):1087–1092, 1953.
- 666 [80] W Keith Hastings. Monte carlo sampling methods using markov chains and their applications.
667 1970.
- 668 [81] Mark Girolami and Ben Calderhead. Riemann manifold langevin and hamiltonian monte
669 carlo methods. *Journal of the Royal Statistical Society: Series B (Statistical Methodology)*,
670 73(2):123–214, 2011.

- 671 [82] Andrew Golightly and Darren J Wilkinson. Bayesian parameter inference for stochastic bio-
672 chemical network models using particle markov chain monte carlo. *Interface focus*, 1(6):807–
673 820, 2011.
- 674 [83] Dustin Tran, Rajesh Ranganath, and David Blei. Hierarchical implicit models and likelihood-
675 free variational inference. In *Advances in Neural Information Processing Systems*, pages
676 5523–5533, 2017.
- 677 [84] Sean R Bittner, Agostina Palmigiano, Kenneth D Miller, and John P Cunningham. Degener-
678 ate solution networks for theoretical neuroscience. *Computational and Systems Neuroscience
679 Meeting (COSYNE), Lisbon, Portugal*, 2019.
- 680 [85] Sean R Bittner, Alex T Piet, Chunyu A Duan, Agostina Palmigiano, Kenneth D Miller,
681 Carlos D Brody, and John P Cunningham. Examining models in theoretical neuroscience
682 with degenerate solution networks. *Bernstein Conference 2019, Berlin, Germany*, 2019.
- 683 [86] Marcel Nonnenmacher, Pedro J Goncalves, Giacomo Bassetto, Jan-Matthis Lueckmann, and
684 Jakob H Macke. Robust statistical inference for simulation-based models in neuroscience. In
685 *Bernstein Conference 2018, Berlin, Germany*, 2018.
- 686 [87] Deistler Michael, , Pedro J Goncalves, Kaan Oecal, and Jakob H Macke. Statistical infer-
687 ence for analyzing sloppiness in neuroscience models. In *Bernstein Conference 2019, Berlin,
688 Germany*, 2019.
- 689 [88] Jan-Matthis Lueckmann, Pedro J Goncalves, Giacomo Bassetto, Kaan Öcal, Marcel Nonnen-
690 macher, and Jakob H Macke. Flexible statistical inference for mechanistic models of neural
691 dynamics. In *Advances in Neural Information Processing Systems*, pages 1289–1299, 2017.
- 692 [89] Martin J Wainwright, Michael I Jordan, et al. Graphical models, exponential families, and
693 variational inference. *Foundations and Trends® in Machine Learning*, 1(1–2):1–305, 2008.
- 694 [90] Sean R Bittner and John P Cunningham. Approximating exponential family models (not
695 single distributions) with a two-network architecture. *arXiv preprint arXiv:1903.07515*, 2019.
- 696 [91] Johan Karlsson, Milena Anguelova, and Mats Jirstrand. An efficient method for structural
697 identifiability analysis of large dynamic systems. *IFAC Proceedings Volumes*, 45(16):941–946,
698 2012.

- 699 [92] Ricky TQ Chen, Yulia Rubanova, Jesse Bettencourt, and David K Duvenaud. Neural ordinary
700 differential equations. In *Advances in neural information processing systems*, pages 6571–6583,
701 2018.
- 702 [93] Xuechen Li, Ting-Kam Leonard Wong, Ricky TQ Chen, and David Duvenaud. Scalable
703 gradients for stochastic differential equations. *arXiv preprint arXiv:2001.01328*, 2020.
- 704 [94] Andreas Raue, Clemens Kreutz, Thomas Maiwald, Julie Bachmann, Marcel Schilling, Ursula
705 Klingmüller, and Jens Timmer. Structural and practical identifiability analysis of partially
706 observed dynamical models by exploiting the profile likelihood. *Bioinformatics*, 25(15):1923–
707 1929, 2009.
- 708 [95] Dhruva V Raman, James Anderson, and Antonis Papachristodoulou. Delineating parameter
709 unidentifiabilities in complex models. *Physical Review E*, 95(3):032314, 2017.
- 710 [96] Maria Pia Saccomani, Stefania Audoly, and Leontina D’Angiò. Parameter identifiability of
711 nonlinear systems: the role of initial conditions. *Automatica*, 39(4):619–632, 2003.
- 712 [97] George Papamakarios, Eric Nalisnick, Danilo Jimenez Rezende, Shakir Mohamed, and Bal-
713 aji Lakshminarayanan. Normalizing flows for probabilistic modeling and inference. *arXiv
714 preprint arXiv:1912.02762*, 2019.
- 715 [98] Durk P Kingma and Prafulla Dhariwal. Glow: Generative flow with invertible 1x1 convolu-
716 tions. In *Advances in neural information processing systems*, pages 10215–10224, 2018.
- 717 [99] Durk P Kingma, Tim Salimans, Rafal Jozefowicz, Xi Chen, Ilya Sutskever, and Max Welling.
718 Improved variational inference with inverse autoregressive flow. *Advances in neural informa-
719 tion processing systems*, 29:4743–4751, 2016.
- 720 [100] Diederik P Kingma and Jimmy Ba. Adam: A method for stochastic optimization. *Internation-
721 al Conference on Learning Representations*, 2015.
- 722 [101] Emmanuel Klinger, Dennis Rickert, and Jan Hasenauer. pyabc: distributed, likelihood-free
723 inference. *Bioinformatics*, 34(20):3591–3593, 2018.
- 724 [102] David S Greenberg, Marcel Nonnenmacher, and Jakob H Macke. Automatic posterior trans-
725 formation for likelihood-free inference. *International Conference on Machine Learning*, 2019.

726 **5 Methods**

727 **5.1 Emergent property inference (EPI)**

728 Determining the combinations of model parameters that can produce observed data or a desired
729 output is a key part of scientific practice. Solving inverse problems is especially important in
730 neuroscience, since we require complex models to describe the complex phenomena of neural com-
731 putations. While much machine learning research has focused on how to find latent structure
732 in large-scale neural datasets, less has focused on inverting theoretical circuit models conditioned
733 upon the emergent phenomena they produce. Here, we introduce a novel method for statistical
734 inference, which finds distributions of parameter solutions that only produce the desired emer-
735 gent property. This method seamlessly handles neural circuit models with stochastic nonlinear
736 dynamical generative processes, which are predominant in theoretical neuroscience.

737 Consider model parameterization \mathbf{z} , which is a collection of scientifically interesting variables that
738 govern the complex simulation of data \mathbf{x} . For example (see Section 3.1), \mathbf{z} may be the electrical
739 conductance parameters of an STG subcircuit, and \mathbf{x} the evolving membrane potentials of the five
740 neurons. In terms of statistical modeling, this circuit model has an intractable likelihood $p(\mathbf{x} | \mathbf{z})$,
741 which is predicated by the stochastic differential equations that define the model. Even so, we do
742 not scientifically reason about how \mathbf{z} governs all of \mathbf{x} , but rather specific phenomena that are a
743 function of the data $f(\mathbf{x}; \mathbf{z})$. In the STG example, $f(\mathbf{x}; \mathbf{z})$ measures hub neuron frequency from the
744 evolution of \mathbf{x} governed by \mathbf{z} . With EPI, we learn distributions of \mathbf{z} that results in an average and
745 variance of $f(\mathbf{x}; \mathbf{z})$, denoted $\boldsymbol{\mu}$ and σ^2 . We refer to the collection of these statistical moments as an
746 emergent property. Such emergent properties \mathcal{X} are defined through choice of $f(\mathbf{x}; \mathbf{z})$ (which may
747 be one or multiple statistics), $\boldsymbol{\mu}$, and σ^2

$$\mathcal{X} : \mathbb{E}_{\mathbf{z}, \mathbf{x}} [f(\mathbf{x}; \mathbf{z})] = \boldsymbol{\mu}, \text{Var}_{\mathbf{z}, \mathbf{x}} [f(\mathbf{x}; \mathbf{z})] = \sigma^2. \quad (11)$$

748 Precisely, the emergent property statistics $f(\mathbf{x}; \mathbf{z})$ must have means $\boldsymbol{\mu}$ and variances σ^2 over the
749 EPI distribution of parameters and stochasticity of the data given the parameters. By defining
750 these means and variances over both levels of stochasticity – the inferred distribution and that of
751 the model – there is a fine degree of control over predictions made by the inferred parameters.
752 In EPI, deep probability distributions are optimized to learn the inferred distribution. In deep
753 probability distributions, a simple random variable $\mathbf{z}_0 \sim q_0(\mathbf{z}_0)$ is mapped deterministically via a
754 sequence of deep neural network layers (g_1, \dots, g_l) parameterized by weights and biases $\boldsymbol{\theta}$ to the

755 support of the distribution of interest:

$$\mathbf{z} = g_{\theta}(\mathbf{z}_0) = g_l(\dots g_1(\mathbf{z}_0)) \sim q_{\theta}(\mathbf{z}). \quad (12)$$

756 Such deep probability distributions embed the inferred distribution in a deep network. Once opti-
757 mized, this deep network representation has remarkably useful properties: fast sampling, probability
758 evaluations, and also first- and second-order probability gradient evaluations.

759 By choosing a neural circuit model, often represented as a system of differential equations, we
760 implicitly define a model likelihood $p(\mathbf{x} | \mathbf{z})$, which may be unknown or intractable for our purposes.
761 Given this model choice and that of an emergent property \mathcal{X} , $q_{\theta}(\mathbf{z})$ is optimized via the neural
762 network parameters θ to find a maximally entropic distribution q_{θ}^* within the deep variational
763 family \mathcal{Q} producing the emergent property \mathcal{X} :

$$q_{\theta}(\mathbf{z} | \mathcal{X}) = q_{\theta}^*(\mathbf{z}) = \operatorname{argmax}_{q_{\theta} \in \mathcal{Q}} H(q_{\theta}(\mathbf{z})) \quad (13)$$
$$\text{s.t. } \mathcal{X} : \mathbb{E}_{\mathbf{z}, \mathbf{x}} [f(\mathbf{x}; \mathbf{z})] = \boldsymbol{\mu}, \operatorname{Var}_{\mathbf{z}, \mathbf{x}} [f(\mathbf{x}; \mathbf{z})] = \boldsymbol{\sigma}^2.$$

764 Entropy is chosen as the normative selection principle to match that of Bayesian inference (see
765 Section 5.1.5). However, a key difference is that variational inference and other Bayesian methods
766 do not constrain the predictions of their inferred parameter distribution. This optimization is
767 executed using the algorithm of Maximum Entropy Flow Networks (MEFNs) [47].

768 In the remainder of Section 5.1, we will explain the finer details and motivation of the EPI method.
769 First, we explain related approaches and what EPI introduces to this domain (Section 5.1.1). Sec-
770 ond, we describe the special class of deep probability distributions used in EPI called normalizing
771 flows (Section 5.1.2). Next, we explain the constrained optimization technique used to solve Equa-
772 tion 13 (Section 5.1.3). Then, we demonstrate the details of this optimization in a toy example
773 (Section 5.1.4). Finally, we establish the known relationship between maximum entropy distribu-
774 tions and exponential families (Section 5.1.5), which is used to explain how EPI can be viewed as
775 a form of variational inference (Section 5.1.6).

776 5.1.1 Related approaches

777 When Bayesian inference problems lack conjugacy, scientists use approximate inference methods like
778 variational inference (VI) [46] and Markov chain Monte Carlo (MCMC) [79, 80]. After optimization,
779 variational methods return a parameterized posterior distribution, which we can analyze. Also, the
780 variational approximating distribution class is often chosen such that it permits fast sampling. In

781 contrast MCMC methods only produce samples from the approximated posterior distribution. No
782 parameterized distribution is estimated, and additional samples are always generated with the same
783 sampling complexity. Inference in models defined by systems of differential has been demonstrated
784 with MCMC [81], although this approach requires tractable likelihoods. Advancements have lever-
785 aged structure in stochastic differential equation models to improve likelihood approximations, thus
786 expanding the domain of applicable models [82].

787 Likelihood-free (or ‘simulation-based’) inference (LFI) [66] is model parameter inference in the
788 absence of a tractable likelihood function. The most prevalent approach to LFI is approximate
789 Bayesian computation [77], in which satisfactory parameter samples are kept from random prior
790 sampling according to a rejection heuristic. The obtained set of parameters do not have a prob-
791 abilities, and further insight about the model must be gained from examination of the parameter
792 set and their generated activity. Methodological advances to ABC methods have come through the
793 use of Markov chain Monte Carlo (MCMC-ABC) [78] and sequential Monte Carlo (SMC-ABC) [41]
794 sampling techniques. SMC-ABC is considered state-of-the-art ABC, yet this approach still strug-
795 gles to scale in dimensionality (cf. Fig. 2). Furthermore, once a parameter set has been obtained by
796 SMC-ABC from a finite set of particles, the SMC-ABC algorithm must be run again from scratch
797 with a new population of initialized particles to obtain additional samples.

798 For scientific model analysis, we seek a parameter distribution exhibiting the properties of a well-
799 chosen variational approximation: a parametric form conferring analytic calculations, and trivial
800 sampling time. For this reason, ABC and MCMC techniques are unattractive, since they only
801 produce a set of parameter samples and have unchanging sampling rate. EPI infers parameters
802 in likelihood-free models using the MEFN [47] algorithm using a deep variational approximation.
803 The deep neural network of EPI defines the parametric form of the distribution approximation.
804 Furthermore, the EPI distribution is constrained to produce an emergent property. In other words,
805 the summary statistics of the posterior predictive distribution are fixed to have certain first and
806 second moments. EPI optimization is enabled using stochastic gradient techniques in the spirit
807 of likelihood-free variational inference [83]. The analytic relationship between EPI and variational
808 inference is explained in Secton 5.1.6.

809 We note that, during our preparation and early presentation of this work [84, 85], another work
810 has arisen with broadly similar goals: bringing statistical inference to mechanistic models of neural
811 circuits ([43, 86, 87]). We are encouraged by this general problem being recognized by others in the
812 community, and we emphasize that these works offer complementary neuroscientific contributions

813 (different theoretical models of focus) and use different technical methodologies (ours is built on
814 our prior work [47], theirs similarly [88]).

815 The method EPI differs from SNPE in some key ways. SNPE belongs to a “sequential” class of
816 recently developed LFI methods in which two neural networks are used for posterior inference.
817 This first neural network is a deep probability distribution (normalizing flow) used to estimate the
818 posterior $p(\mathbf{z} | \mathbf{x})$ (SNPE) or the likelihood $p(\mathbf{x} | \mathbf{z})$ (sequential neural likelihood (SNL [44])). A
819 recent advance uses an unconstrained neural network to estimate the likelihood ratio (sequential
820 neural ratio estimation (SNRE [45])). In SNL and SNRE, MCMC sampling techniques are used to
821 obtain samples from the approximated posterior. This contrasts with EPI and SNPE, which use
822 deep probability distributions to model parameters, which facilitates immediate measurements of
823 sample probability, gradient, or Hessian for system analysis. The second neural network in this
824 sequential class of methods is the amortizer. This unconstrained deep network maps data \mathbf{x} (or
825 statistics $f(\mathbf{x}; \mathbf{z})$ or model parameters \mathbf{z} to the weights and biases of the first neural network. These
826 methods are optimized on a conditional density (or ratio) estimation objective. The data used to
827 optimize this objective are generated via an adaptive procedure, in which training data pairs $(\mathbf{x}_i,$
828 $\mathbf{z}_i)$ become sequentially closer to the true data and posterior.

829 The approximating fidelity of the deep probability distribution in sequential approaches is optimized
830 to generalize across the training distribution of the conditioning variable. This generalization prop-
831 erty of the sequential methods can reduce the accuracy at the singular posterior of interest. Whereas
832 in EPI, the entire expressivity of the deep probability distribution is dedicated to learning a single
833 distribution as well as possible. Amortization is not possible in EPI, since EPI learns an expo-
834 nential family distribution parameterized by its mean (see Section 5.1.5). Since EPI distributions
835 are defined by the mean μ of their statistics, there is the well-known inverse mapping problem of
836 exponential families [89] that prohibits an amortization based approach. However, we have shown
837 that the same two-network architecture of the sequential LFI methods can be used for amortized
838 inference in intractable exponential family posteriors using their natural parameterization [90].

839 Finally, one important differentiating factor between EPI and sequential LFI methods is that EPI
840 leverages gradients $\nabla_{\mathbf{z}} f(\mathbf{x}; \mathbf{z})$ during optimization. These gradients can improve convergence time
841 and scalability, as we have shown on an example conditioning low-rank RNN connectivity on the
842 property of stable amplification (see Section 3.3). With EPI, we prove out the suggestion that a
843 deep inference technique can improve efficiency by leveraging these model gradients when they are
844 tractable. Sequential LFI techniques may be better suited for scientific problems where $\nabla_{\mathbf{z}} f(\mathbf{x}; \mathbf{z})$ is

845 intractable or unavailable: when there is a nondifferentiable model or it requires lengthy simulations.
846 However, the sequential LFI techniques cannot constrain the predictions of the inferred distribution
847 in the manner of EPI.

848 Structural identifiability analysis involves the measurement of sensitivity and unidentifiabilities in
849 natural models. Around a point, one can measure the Jacobian. One approach that scales well is
850 EAR [91]. A popular efficient approach for systems of ODEs has been neural ODE adjoint [92] and
851 its stochastic adaptation [93]. Casting identifiability as a statistical estimation problem, the profile
852 likelihood can assess via iterated optimization while holding parameters fixed [94]. An exciting
853 recent method is capable of recovering the functional form of such unidentifiabilities away from a
854 point by following degenerate dimensions of the fisher information matrix [95]. Global structural
855 non-identifiabilities can be found for models with polynomial or rational dynamics equations using
856 DAISY [96]. With EPI, we have all the benefits given by a statistical inference method plus the
857 ability to query the first- or second-order gradient of the probability of the inferred distribution at
858 any chosen parameter value. The second-order gradient of the log probability (the Hessian), which
859 is directly afforded by EPI distributions, produces salient information about parametric sensitivity
860 of the emergent property. For example, the eigenvector with most negative eigenvalue of the Hessian
861 shows parametric combinations away from a parameter choice that decrease the in EPI distribution
862 probability the fastest. We refer to this eigenvector as the sensitivity dimension, and it is used to
863 generate scientific insight about a model of superior colliculus connectivity (see Section 3.5).

864 **5.1.2 Deep probability distributions and normalizing flows**

865 Deep probability distributions are comprised of multiple layers of fully connected neural networks
866 (Equation 12). When each neural network layer is restricted to be a bijective function, the sample
867 density can be calculated using the change of variables formula at each layer of the network. For
868 $\mathbf{z}_i = g_i(\mathbf{z}_{i-1})$,

$$p(\mathbf{z}_i) = p(g_i^{-1}(\mathbf{z}_i)) \left| \det \frac{\partial g_i^{-1}(\mathbf{z}_i)}{\partial \mathbf{z}_i} \right| = p(\mathbf{z}_{i-1}) \left| \det \frac{\partial g_i(\mathbf{z}_{i-1})}{\partial \mathbf{z}_{i-1}} \right|^{-1}. \quad (14)$$

869 However, this computation has cubic complexity in dimensionality for fully connected layers. By
870 restricting our layers to normalizing flows [48, 97] – bijective functions with fast log determinant
871 Jacobian computations, which confer a fast calculation of the sample log probability. Fast log
872 probability calculation confers efficient optimization of the maximum entropy objective (see Section
873 5.1.3). We use the Real NVP [58] normalizing flow class, because its coupling architecture confers

874 both fast sampling (forward) and fast log probability evaluation (backward). Fast probability
 875 evaluation in turn facilitates fast gradient and Hessian evaluation of log probability throughout
 876 parameter space. Glow permutations were used in between coupling stages [98]. This is in contrast
 877 to autoregressive architectures [59, 99], in which only one of the forward or backward passes can
 878 be efficient. In this work, normalizing flows are used as flexible posterior approximations $q_{\theta}(\mathbf{z})$
 879 having weights and biases θ . We specify the architecture used in each application by the number
 880 of Real-NVP affine coupling stages, and the number of neural network layers and units per layer
 881 of the conditioning functions.

882 5.1.3 Augmented Lagrangian optimization

883 To optimize $q_{\theta}(\mathbf{z})$ in Equation 13, the constrained maximum entropy optimization is executed using
 884 the augmented Lagrangian method. The following objective is minimized:

$$L(\theta; \eta_{\text{opt}}, c) = -H(q_{\theta}) + \eta_{\text{opt}}^T R(\theta) + \frac{c}{2} \|R(\theta)\|^2 \quad (15)$$

885 where average constraint violations $R(\theta) = \mathbb{E}_{\mathbf{z} \sim q_{\theta}} [\mathbb{E}_{\mathbf{x} \sim p(\mathbf{x}|\mathbf{z})} [T(\mathbf{x}; \mathbf{z}) - \mu_{\text{opt}}]]$, $\eta_{\text{opt}} \in \mathbb{R}^m$ are the
 886 Lagrange multipliers where $m = |\mu_{\text{opt}}| = |T(\mathbf{x}; \mathbf{z})| = 2|f(\mathbf{x}; \mathbf{z})|$, and c is the penalty coefficient. The
 887 sufficient statistics $T(\mathbf{x}; \mathbf{z})$ and mean parameter μ_{opt} are determined by the means μ and variances
 888 σ^2 of emergent property statistics $f(\mathbf{x}; \mathbf{z})$ defined in Equation 13 (see Section 5.1.6). Specifically,
 889 $T(\mathbf{x}; \mathbf{z})$ is a concatenation of the first and second moments, μ_{opt} is a concatenation of μ and σ^2
 890 (see section 5.1.5), and the Lagrange multipliers are closely related to the natural parameters η of
 891 exponential families (see Section 5.1.5). Weights and biases θ of the deep probability distribution
 892 are optimized according to Equation 15 using the Adam optimizer with learning rate 10^{-3} [100].

893 The gradient with respect to entropy $H(q_{\theta}(\mathbf{z}))$ can be expressed using the reparameterization trick
 894 as an expectation of the negative log density of parameter samples \mathbf{z} over the randomness in the
 895 parameterless initial distribution $q_0(\mathbf{z}_0)$:

$$H(q_{\theta}(\mathbf{z})) = \int -q_{\theta}(\mathbf{z}) \log(q_{\theta}(\mathbf{z})) d\mathbf{z} = \mathbb{E}_{\mathbf{z} \sim q_{\theta}} [-\log(q_{\theta}(\mathbf{z}))] = \mathbb{E}_{\mathbf{z}_0 \sim q_0} [-\log(q_{\theta}(g_{\theta}(\mathbf{z}_0)))]. \quad (16)$$

896 Thus, the gradient of the entropy of the deep probability distribution can be estimated as an
 897 average with respect to the base distribution \mathbf{z}_0 :

$$\nabla_{\theta} H(q_{\theta}(\mathbf{z})) = \mathbb{E}_{\mathbf{z}_0 \sim q_0} [-\nabla_{\theta} \log(q_{\theta}(g_{\theta}(\mathbf{z}_0)))]. \quad (17)$$

898 The lagrangian parameters η_{opt} are initialized to zero and adapted following each augmented
 899 Lagrangian epoch, which is a period of optimization with fixed (η_{opt}, c) for a given number of

900 stochastic optimization iterations. A low value of c is used initially, and conditionally increased
901 after each epoch based on constraint error reduction. The penalty coefficient is updated based
902 on the result of a hypothesis test regarding the reduction in constraint violation. The p-value of
903 $\mathbb{E}[|R(\boldsymbol{\theta}_{k+1})|] > \gamma \mathbb{E}[|R(\boldsymbol{\theta}_k)|]$ is computed, and c_{k+1} is updated to βc_k with probability $1 - p$. The
904 other update rule is $\boldsymbol{\eta}_{\text{opt},k+1} = \boldsymbol{\eta}_{\text{opt},k} + c_k \frac{1}{n} \sum_{i=1}^n (T(\mathbf{x}^{(i)}) - \boldsymbol{\mu}_{\text{opt}})$ given a batch size n . Throughout
905 the study, $\gamma = 0.25$, while β was chosen to be either 2 or 4. The batch size of EPI also varied
906 according to application.

907 The intention is that c and $\boldsymbol{\eta}_{\text{opt}}$ start at values encouraging entropic growth early in optimization.
908 With each training epoch in which the update rule for c is invoked by unsatisfactory constraint
909 error reduction, the constraint satisfaction terms are increasingly weighted, resulting in a decreased
910 entropy. This encourages the discovery of suitable regions of parameter space, and the subsequent
911 refinement of the distribution to produce the emergent property (see example in Section 5.1.4). The
912 momentum parameters of the Adam optimizer are reset at the end of each augmented Lagrangian
913 epoch.

914 Rather than starting optimization from some $\boldsymbol{\theta}$ drawn from a randomized distribution, we found
915 that initializing $q_{\boldsymbol{\theta}}(\mathbf{z})$ to approximate an isotropic Gaussian distribution conferred more stable, con-
916 sistent optimization. The parameters of the Gaussian initialization were chosen on an application-
917 specific basis. Throughout the study, we chose isotropic Gaussian initializations with mean $\boldsymbol{\mu}_{\text{init}}$
918 at the center of the distribution support and some standard deviation σ_{init} , except for one case,
919 where an initialization informed by random search was used (see Section 5.2.1).

920 To assess whether the EPI distribution $q_{\boldsymbol{\theta}}(\mathbf{z})$ produces the emergent property, we assess whether
921 each individual constraint on the means and variances of $f(\mathbf{x}; \mathbf{z})$ is satisfied. We consider the EPI
922 to have converged when a null hypothesis test of constraint violations $R(\boldsymbol{\theta})_i$ being zero is accepted
923 for all constraints $i \in \{1, \dots, m\}$ at a significance threshold $\alpha = 0.05$. This significance threshold is
924 adjusted through Bonferroni correction according to the number of constraints m . The p-values for
925 each constraint are calculated according to a two-tailed nonparametric test, where 200 estimations
926 of the sample mean $R(\boldsymbol{\theta})^i$ are made using N_{test} samples of $\mathbf{z} \sim q_{\boldsymbol{\theta}}(\mathbf{z})$ at the end of the augmented
927 Lagrangian epoch.

928 When assessing the suitability of EPI for a particular modeling question, there are some important
929 technical considerations. First and foremost, as in any optimization problem, the defined emergent
930 property should always be appropriately conditioned (constraints should not have wildly different
931 units). Furthermore, if the program is underconstrained (not enough constraints), the distribution

grows (in entropy) unstably unless mapped to a finite support. If overconstrained, there is no parameter set producing the emergent property, and EPI optimization will fail (appropriately). Next, one should consider the computational cost of the gradient calculations. In the best circumstance, there is a simple, closed form expression (e.g. Section 5.2.2) for the emergent property statistic given the model parameters. On the other end of the spectrum, many forward simulation iterations may be required before a high quality measurement of the emergent property statistic is available (e.g. Section 5.2.1). In such cases, backpropagating gradients through the SDE evolution will be expensive.

5.1.4 Example: 2D LDS

To gain intuition for EPI, consider a two-dimensional linear dynamical system (2D LDS) model (Fig. S1A):

$$\tau \frac{d\mathbf{x}}{dt} = A\mathbf{x} \quad (18)$$

with

$$A = \begin{bmatrix} a_1 & a_2 \\ a_3 & a_4 \end{bmatrix}. \quad (19)$$

To run EPI with the dynamics matrix elements as the free parameters $\mathbf{z} = [a_1, a_2, a_3, a_4]$ (fixing $\tau = 1$), the emergent property statistics $T(\mathbf{x})$ were chosen to contain the first and second moments of the oscillatory frequency, $\frac{\text{imag}(\lambda_1)}{2\pi}$, and the growth/decay factor, $\text{real}(\lambda_1)$, of the oscillating system. λ_1 is the eigenvalue of greatest real part when the imaginary component is zero, and alternatively of positive imaginary component when the eigenvalues are complex conjugate pairs. To learn the distribution of real entries of A that produce a band of oscillating systems around 1Hz, we formalized this emergent property as $\text{real}(\lambda_1)$ having mean zero with variance 0.25^2 , and the oscillation frequency $2\pi\text{imag}(\lambda_1)$ having mean $\omega = 1$ Hz with variance $(0.1\text{Hz})^2$:

$$\mathbb{E}[T(\mathbf{x})] \triangleq \mathbb{E} \begin{bmatrix} \text{real}(\lambda_1) \\ \text{imag}(\lambda_1) \\ (\text{real}(\lambda_1) - 0)^2 \\ (\text{imag}(\lambda_1) - 2\pi\omega)^2 \end{bmatrix} = \begin{bmatrix} 0.0 \\ 2\pi\omega \\ 0.25^2 \\ (2\pi 0.1)^2 \end{bmatrix} \triangleq \boldsymbol{\mu}. \quad (20)$$

952

Unlike the models we presented in the main text, this model admits an analytical form for the mean emergent property statistics given parameter \mathbf{z} , since the eigenvalues can be calculated using

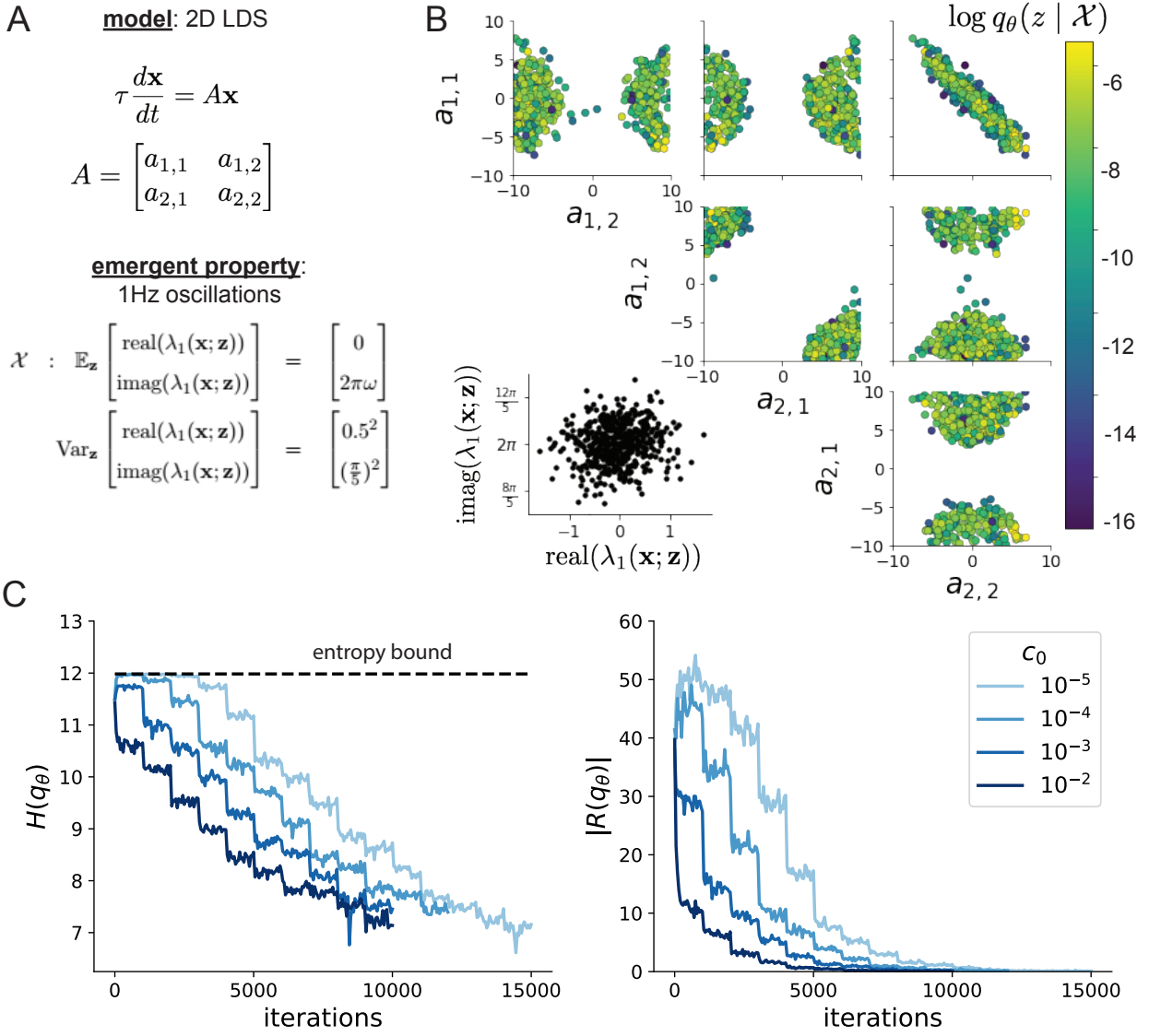


Figure 6: (LDS1): **A.** Two-dimensional linear dynamical system model, where real entries of the dynamics matrix A are the parameters. **B.** The EPI distribution for a two-dimensional linear dynamical system with $\tau = 1$ that produces an average of 1Hz oscillations with some small amount of variance. Dashed lines indicate the parameter axes. **C.** Entropy throughout the optimization. At the beginning of each augmented Lagrangian epoch (2,000 iterations), the entropy dipped due to the shifted optimization manifold where emergent property constraint satisfaction is increasingly weighted. **D.** Emergent property moments throughout optimization. At the beginning of each augmented Lagrangian epoch, the emergent property moments adjust closer to their constraints.

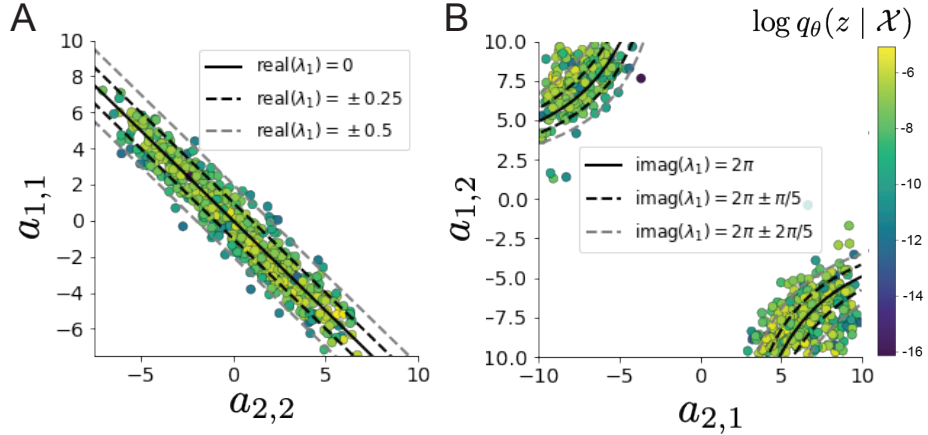


Figure 7: (LDS2): **A.** Probability contours in the a_1 - a_4 plane were derived from the relationship to emergent property statistic of growth/decay factor $\text{real}(\lambda_1)$. **B.** Probability contours in the a_2 - a_3 plane were derived from the emergent property statistic of oscillation frequency $2\pi\text{imag}(\lambda_1)$.

955 the quadratic formula:

$$\lambda = \frac{\left(\frac{a_1+a_4}{\tau}\right) \pm \sqrt{\left(\frac{a_1+a_4}{\tau}\right)^2 + 4\left(\frac{a_2a_3-a_1a_4}{\tau}\right)}}{2}. \quad (21)$$

956 Importantly, even though $\mathbb{E}_{\mathbf{x} \sim p(\mathbf{x}|\mathbf{z})}[T(\mathbf{x})]$ is calculable directly via a closed form function and
957 does not require simulation, we cannot derive the distribution q_θ^* directly. This fact is due to the
958 formally hard problem of the backward mapping: finding the natural parameters η from the mean
959 parameters μ of an exponential family distribution [89]. Instead, we used EPI to approximate this
960 distribution (Fig. S1B). We used a real-NVP normalizing flow architecture with four masks, two
961 neural network layers of 15 units per mask, with batch normalization momentum 0.99, mapped
962 onto a support of $z_i \in [-10, 10]$. (see Section 5.1.2).

963 Even this relatively simple system has nontrivial (though intuitively sensible) structure in the
964 parameter distribution. To validate our method, we analytically derived the contours of the prob-
965 ability density from the emergent property statistics and values. In the a_1 - a_4 plane, the black
966 line at $\text{real}(\lambda_1) = \frac{a_1+a_4}{2} = 0$, dotted black line at the standard deviation $\text{real}(\lambda_1) = \frac{a_1+a_4}{2} \pm 0.25$,
967 and the dotted gray line at twice the standard deviation $\text{real}(\lambda_1) = \frac{a_1+a_4}{2} \pm 0.5$ follow the contour
968 of probability density of the samples (Fig. S2A). The distribution precisely reflects the desired
969 statistical constraints and model degeneracy in the sum of a_1 and a_4 . Intuitively, the parameters
970 equivalent with respect to emergent property statistic $\text{real}(\lambda_1)$ have similar log densities.

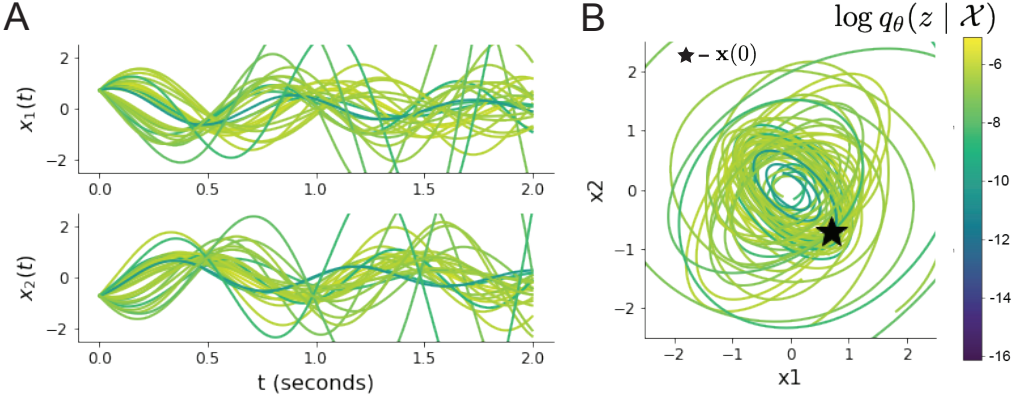


Figure 8: (LDS3): Sampled dynamical systems $\mathbf{z} \sim q_{\theta}(\mathbf{z})$ and their simulated activity from $\mathbf{x}(0) = [\frac{\sqrt{2}}{2}, -\frac{\sqrt{2}}{2}]$ colored by log probability. **A.** Each dimension of the simulated trajectories throughout time. **B.** The simulated trajectories in phase space.

971 To explain the bimodality of the EPI distribution, we examined the imaginary component of λ_1 .
 972 When $\text{real}(\lambda_1) = \frac{a_1 + a_4}{2} = 0$, we have

$$\text{imag}(\lambda_1) = \begin{cases} \sqrt{\frac{a_1 a_4 - a_2 a_3}{\tau}}, & \text{if } a_1 a_4 < a_2 a_3 \\ 0 & \text{otherwise} \end{cases}. \quad (22)$$

973 When $\tau = 1$ and $a_1 a_4 > a_2 a_3$ (center of distribution above), we have the following equation for the
 974 other two dimensions:

$$\text{imag}(\lambda_1)^2 = a_1 a_4 - a_2 a_3 \quad (23)$$

975 Since we constrained $\mathbb{E}_{\mathbf{z} \sim q_{\theta}} [\text{imag}(\lambda)] = 2\pi$ (with $\omega = 1$), we can plot contours of the equation
 976 $\text{imag}(\lambda_1)^2 = a_1 a_4 - a_2 a_3 = (2\pi)^2$ for various $a_1 a_4$ (Fig. S2B). With $\sigma_{1,4} = \mathbb{E}_{\mathbf{z} \sim q_{\theta}} (|a_1 a_4 - E_{q_{\theta}}[a_1 a_4]|)$,
 977 we show the contours as $a_1 a_4 = 0$ (black), $a_1 a_4 = -\sigma_{1,4}$ (black dotted), and $a_1 a_4 = -2\sigma_{1,4}$ (grey
 978 dotted). This validates the curved structure of the inferred distribution learned through EPI. We
 979 took steps in negative standard deviation of $a_1 a_4$ (dotted and gray lines), since there are few positive
 980 values $a_1 a_4$ in the learned distribution. Subtler combinations of model and emergent property will
 981 have more complexity, further motivating the use of EPI for understanding these systems. As we
 982 expect, the distribution results in samples of two-dimensional linear systems oscillating near 1Hz
 983 (Fig. S3).

984 **5.1.5 Maximum entropy distributions and exponential families**

985 EPI is a maximum entropy distribution, which have fundamental links to exponential family dis-
 986 tributions. A maximum entropy distribution of form:

$$p^*(\mathbf{z}) = \underset{p \in \mathcal{P}}{\operatorname{argmax}} H(p(\mathbf{z})) \quad (24)$$

s.t. $\mathbb{E}_{\mathbf{z} \sim p}[T(\mathbf{z})] = \boldsymbol{\mu}_{\text{opt}}.$

987 will have probability density in the exponential family:

$$p^*(\mathbf{z}) \propto \exp(\boldsymbol{\eta}^\top T(\mathbf{z})). \quad (25)$$

988 The mappings between the mean parameterization $\boldsymbol{\mu}_{\text{opt}}$ and the natural parameterization $\boldsymbol{\eta}$ are
 989 formally hard to identify except in special cases [89].

990 In EPI, emergent properties are defined as statistics having a fixed mean and variance as in Equation
 991 4. The variance constraint is a second moment constraint on $f(\mathbf{x}; \mathbf{z})$

$$\operatorname{Var}_{\mathbf{z}, \mathbf{x}}[f(\mathbf{x}; \mathbf{z})] = \mathbb{E}_{\mathbf{z}, \mathbf{x}}[(f(\mathbf{x}; \mathbf{z}) - \boldsymbol{\mu})^2] \quad (26)$$

992 As a general maximum entropy distribution (Equation 24), the sufficient statistics vector contains
 993 both first and second order moments of $f(\mathbf{x}; \mathbf{z})$

$$T(\mathbf{x}; \mathbf{z}) = \begin{bmatrix} f(\mathbf{x}; \mathbf{z}) \\ (f(\mathbf{x}; \mathbf{z}) - \boldsymbol{\mu})^2 \end{bmatrix}, \quad (27)$$

994 which are constrained to the chosen means and variances

$$\boldsymbol{\mu}_{\text{opt}} = \begin{bmatrix} \boldsymbol{\mu} \\ \sigma^2 \end{bmatrix}. \quad (28)$$

995 **5.1.6 EPI as variational inference**

996 In Bayesian inference a prior belief about model parameters \mathbf{z} is stated in a prior distribution $p(\mathbf{z})$,
 997 and the statistical model capturing the effect of \mathbf{z} on observed data points \mathbf{x} is formalized in the
 998 likelihood distribution $p(\mathbf{x} | \mathbf{z})$. In Bayesian inference, we obtain a posterior distribution $p(\mathbf{z} | \mathbf{x})$,
 999 which captures how the data inform our knowledge of model parameters using Bayes' rule:

$$p(\mathbf{z} | \mathbf{x}) = \frac{p(\mathbf{x} | \mathbf{z})p(\mathbf{z})}{p(\mathbf{x})}. \quad (29)$$

1000 The posterior distribution is analytically available when the prior is conjugate with the likelihood.
 1001 However, conjugacy is rare in practice, and alternative methods, such as variational inference [46],
 1002 are utilized.

1003 In variational inference, a posterior approximation q_{θ}^* is chosen from within some variational family
 1004 \mathcal{Q}

$$q_{\theta}^*(\mathbf{z}) = \operatorname{argmin}_{q_{\theta} \in \mathcal{Q}} KL(q_{\theta}(\mathbf{z}) \parallel p(\mathbf{z} \mid \mathbf{x})). \quad (30)$$

1005 The KL divergence can be written in terms of entropy of the variational approximation:

$$KL(q_{\theta}(\mathbf{z}) \parallel p(\mathbf{z} \mid \mathbf{x})) = \mathbb{E}_{\mathbf{z} \sim q_{\theta}} [\log(q_{\theta}(\mathbf{z}))] - \mathbb{E}_{\mathbf{z} \sim q_{\theta}} [\log(p(\mathbf{z} \mid \mathbf{x}))] \quad (31)$$

1006

$$= -H(q_{\theta}) - \mathbb{E}_{\mathbf{z} \sim q_{\theta}} [\log(p(\mathbf{x} \mid \mathbf{z})) + \log(p(\mathbf{z})) - \log(p(\mathbf{x}))] \quad (32)$$

1007 Since the marginal distribution of the data $p(\mathbf{x})$ (or ‘‘evidence’’) is independent of θ , variational
 1008 inference is executed by optimizing the remaining expression. This is usually framed as maximizing
 1009 the evidence lower bound (ELBO)

$$\operatorname{argmin}_{q_{\theta} \in \mathcal{Q}} KL(q_{\theta} \parallel p(\mathbf{z} \mid \mathbf{x})) = \operatorname{argmax}_{q_{\theta} \in \mathcal{Q}} H(q_{\theta}) + \mathbb{E}_{\mathbf{z} \sim q_{\theta}} [\log(p(\mathbf{x} \mid \mathbf{z})) + \log(p(\mathbf{z}))]. \quad (33)$$

1010 Now, consider the setting where we have chosen a uniform prior, and stipulate a mean-field gaussian
 1011 likelihood on a chosen statistic of the data $f(\mathbf{x}; \mathbf{z})$

$$p(\mathbf{x} \mid \mathbf{z}) = \mathcal{N}(f(\mathbf{x}; \mathbf{z}) \mid \boldsymbol{\mu}_f, \Sigma_f), \quad (34)$$

1012 where $\Sigma_f = \operatorname{diag}(\sigma_f^2)$. The log likelihood is then proportional to a dot product of the natural
 1013 parameter of this mean-field gaussian distribution and the first and second moment statistics.

$$\log p(\mathbf{x} \mid \mathbf{z}) \propto \boldsymbol{\eta}_f^\top T(\mathbf{x}, \mathbf{z}), \quad (35)$$

1014 where

$$\boldsymbol{\eta}_f = \begin{bmatrix} \frac{\boldsymbol{\mu}_f}{\sigma_f^2} \\ \frac{-1}{2\sigma_f^2} \end{bmatrix}, \text{ and} \quad (36)$$

1015

$$T(\mathbf{x}; \mathbf{z}) = \begin{bmatrix} f(\mathbf{x}; \mathbf{z}) \\ (f(\mathbf{x}; \mathbf{z}) - \boldsymbol{\mu}_f)^2 \end{bmatrix}. \quad (37)$$

1016 The variational objective is then

$$\operatorname{argmax}_{q_{\theta} \in \mathcal{Q}} H(q_{\theta}) + \boldsymbol{\eta}_f^\top \mathbb{E}_{\mathbf{z} \sim q_{\theta}} [T(\mathbf{x}; \mathbf{z})] \quad (38)$$

1017 Comparing this to the Lagrangian objective (without augmentation) of EPI, we see they are the
 1018 same

$$\begin{aligned} q_{\theta}^*(\mathbf{z}) &= \underset{q_{\theta} \in Q}{\operatorname{argmin}} -H(q_{\theta}) + \boldsymbol{\eta}_{\text{opt}}^\top (\mathbb{E}_{\mathbf{z}, \mathbf{x}} [T(\mathbf{x}; \mathbf{z})] - \boldsymbol{\mu}_{\text{opt}}) \\ &= \underset{q_{\theta} \in Q}{\operatorname{argmin}} -H(q_{\theta}) + \boldsymbol{\eta}_{\text{opt}}^\top \mathbb{E}_{\mathbf{z}, \mathbf{x}} [T(\mathbf{x}; \mathbf{z})]. \end{aligned} \quad (39)$$

1019 where $T(\mathbf{x}; \mathbf{z})$ consists of the first and second moments of the emergent property statistic $f(\mathbf{x}; \mathbf{z})$
 1020 (Equation 27). Thus, EPI is implicitly executing variational inference with a uniform prior and a
 1021 mean-field gaussian likelihood on the emergent property statistics. The mean and variances of the
 1022 mean-field gaussian likelihood are predicated by $\boldsymbol{\eta}_{\text{opt}}$ (Equations 36 and 38), which is adapted after
 1023 each EPI optimization epoch based on \mathcal{X} (see Section 5.1.3). In EPI, the inferred distribution is
 1024 not conditioned on a finite dataset as in variational inference, but rather the emergent property
 1025 \mathcal{X} dictates the likelihood parameterization such that the inferred distribution will produce the
 1026 emergent property. As a note, we could not simply choose $\boldsymbol{\mu}_f$ and $\boldsymbol{\sigma}_f$ directly from the outset, since
 1027 we do not know which of these choices will produce the emergent property \mathcal{X} , which necessitates
 1028 the EPI optimization routine that adapts $\boldsymbol{\eta}_{\text{opt}}$. Accordingly, we replace the notation of $p(\mathbf{z} | \mathbf{x})$
 1029 with $p(\mathbf{z} | \mathcal{X})$ conceptualizing an inferred distribution that obeys emergent property \mathcal{X} (see Section
 1030 5.1).

1031 5.2 Theoretical models

1032 In this study, we used emergent property inference to examine several models relevant to theoretical
 1033 neuroscience. Here, we provide the details of each model and the related analyses.

1034 5.2.1 Stomatogastric ganglion

1035 We analyze how the parameters $\mathbf{z} = [g_{\text{el}}, g_{\text{synA}}]$ govern the emergent phenomena of intermediate
 1036 hub frequency in a model of the stomatogastric ganglion (STG) [50] shown in Figure 1A with
 1037 activity $\mathbf{x} = [x_{\text{f1}}, x_{\text{f2}}, x_{\text{hub}}, x_{\text{s1}}, x_{\text{s2}}]$, using the same hyperparameter choices as Gutierrez et al.
 1038 Each neuron's membrane potential $x_{\alpha}(t)$ for $\alpha \in \{\text{f1}, \text{f2}, \text{hub}, \text{s1}, \text{s2}\}$ is the solution of the following
 1039 stochastic differential equation:

$$C_m \frac{dx_{\alpha}}{dt} = -[h_{\text{leak}}(\mathbf{x}; \mathbf{z}) + h_{Ca}(\mathbf{x}; \mathbf{z}) + h_K(\mathbf{x}; \mathbf{z}) + h_{hyp}(\mathbf{x}; \mathbf{z}) + h_{elec}(\mathbf{x}; \mathbf{z}) + h_{syn}(\mathbf{x}; \mathbf{z})] + dB. \quad (40)$$

1040 The input current of each neuron is the sum of the leak, calcium, potassium, hyperpolarization,
 1041 electrical and synaptic currents as well as gaussian noise dB . Each current component is a function

1042 of all membrane potentials and the conductance parameters \mathbf{z} .

1043 The capacitance of the cell membrane was set to $C_m = 1nF$. Specifically, the currents are the
 1044 difference in the neuron's membrane potential and that current type's reversal potential multiplied
 1045 by a conductance:

$$1046 \quad h_{leak}(\mathbf{x}; \mathbf{z}) = g_{leak}(x_\alpha - V_{leak}) \quad (41)$$

$$1047 \quad h_{elec}(\mathbf{x}; \mathbf{z}) = g_{el}(x_\alpha^{post} - x_\alpha^{pre}) \quad (42)$$

$$1048 \quad h_{syn}(\mathbf{x}; \mathbf{z}) = g_{syn}S_\infty^{pre}(x_\alpha^{post} - V_{syn}) \quad (43)$$

$$1049 \quad h_{Ca}(\mathbf{x}; \mathbf{z}) = g_{Ca}M_\infty(x_\alpha - V_{Ca}) \quad (44)$$

$$1050 \quad h_K(\mathbf{x}; \mathbf{z}) = g_KN(x_\alpha - V_K) \quad (45)$$

$$1051 \quad h_{hyp}(\mathbf{x}; \mathbf{z}) = g_hH(x_\alpha - V_{hyp}). \quad (46)$$

1051 The reversal potentials were set to $V_{leak} = -40mV$, $V_{Ca} = 100mV$, $V_K = -80mV$, $V_{hyp} = -20mV$,
 1052 and $V_{syn} = -75mV$. The other conductance parameters were fixed to $g_{leak} = 1 \times 10^{-4}\mu S$, g_{Ca} ,
 1053 g_K , and g_{hyp} had different values based on fast, intermediate (hub) or slow neuron. The fast
 1054 conductances had values $g_{Ca} = 1.9 \times 10^{-2}$, $g_K = 3.9 \times 10^{-2}$, and $g_{hyp} = 2.5 \times 10^{-2}$. The intermediate
 1055 conductances had values $g_{Ca} = 1.7 \times 10^{-2}$, $g_K = 1.9 \times 10^{-2}$, and $g_{hyp} = 8.0 \times 10^{-3}$. Finally, the
 1056 slow conductances had values $g_{Ca} = 8.5 \times 10^{-3}$, $g_K = 1.5 \times 10^{-2}$, and $g_{hyp} = 1.0 \times 10^{-2}$.

1057 Furthermore, the Calcium, Potassium, and hyperpolarization channels have time-dependent gating
 1058 dynamics dependent on steady-state gating variables M_∞ , N_∞ and H_∞ , respectively:

$$1059 \quad M_\infty = 0.5 \left(1 + \tanh \left(\frac{x_\alpha - v_1}{v_2} \right) \right) \quad (47)$$

$$1060 \quad \frac{dN}{dt} = \lambda_N(N_\infty - N) \quad (48)$$

$$1061 \quad N_\infty = 0.5 \left(1 + \tanh \left(\frac{x_\alpha - v_3}{v_4} \right) \right) \quad (49)$$

$$1062 \quad \lambda_N = \phi_N \cosh \left(\frac{x_\alpha - v_3}{2v_4} \right) \quad (50)$$

$$1063 \quad \frac{dH}{dt} = \frac{(H_\infty - H)}{\tau_h} \quad (51)$$

$$1064 \quad H_\infty = \frac{1}{1 + \exp \left(\frac{x_\alpha + v_5}{v_6} \right)} \quad (52)$$

$$1065 \quad \tau_h = 272 - \left(\frac{-1499}{1 + \exp \left(\frac{-x_\alpha + v_7}{v_8} \right)} \right). \quad (53)$$

1065 where we set $v_1 = 0mV$, $v_2 = 20mV$, $v_3 = 0mV$, $v_4 = 15mV$, $v_5 = 78.3mV$, $v_6 = 10.5mV$,
 1066 $v_7 = -42.2mV$, $v_8 = 87.3mV$, $v_9 = 5mV$, and $v_{th} = -25mV$.

1067 Finally, there is a synaptic gating variable as well:

$$S_\infty = \frac{1}{1 + \exp\left(\frac{v_{th}-x_\alpha}{v_9}\right)}. \quad (54)$$

1068 When the dynamic gating variables are considered, this is actually a 15-dimensional nonlinear
 1069 dynamical system. Gaussian noise $d\mathbf{B}$ of variance $(1 \times 10^{-12})^2 \text{ A}^2$ makes the model stochastic, and
 1070 introduces variability in frequency at each parameterization \mathbf{z} .

1071 In order to measure the frequency of the hub neuron during EPI, the STG model was simulated for
 1072 $T = 300$ time steps of $dt = 25\text{ms}$. The chosen dt and T were the most computationally convenient
 1073 choices yielding accurate frequency measurement. We used a basis of complex exponentials with
 1074 frequencies from 0.0-1.0 Hz at 0.01Hz resolution to measure frequency from simulated time series

$$\Phi = [0.0, 0.01, \dots, 1.0]^\top \dots \quad (55)$$

1075 To measure spiking frequency, we processed simulated membrane potentials with a relu (spike
 1076 extraction) and low-pass filter with averaging window of size 20, then took the frequency with the
 1077 maximum absolute value of the complex exponential basis coefficients of the processed time-series.
 1078 The first 20 temporal samples of the simulation are ignored to account for initial transients.

1079 To differentiate through the maximum frequency identification, we used a soft-argmax Let $X_\alpha \in$
 1080 $\mathcal{C}^{|\Phi|}$ be the complex exponential filter bank dot products with the signal $x_\alpha \in \mathbb{R}^N$, where $\alpha \in$
 1081 $\{\text{f1}, \text{f2}, \text{hub}, \text{s1}, \text{s2}\}$. The soft-argmax is then calculated using temperature parameter $\beta = 100$

$$\psi_\alpha = \text{softmax}(\beta |X_\alpha| \odot i), \quad (56)$$

1082 where $i = [0, 1, \dots, 100]$. The frequency is then calculated as

$$\omega_\alpha = 0.01\psi_\alpha \text{Hz}. \quad (57)$$

1083 Intermediate hub frequency, like all other emergent properties in this work, is defined by the mean
 1084 and variance of the emergent property statistics. In this case, we have one statistic, hub neuron
 1085 frequency, where the mean was chosen to be 0.55Hz, and variance was chosen to be $(0.025\text{Hz})^2$ to
 1086 capture variation in frequency between 0.5Hz and 0.6Hz (Equation 4). As a maximum entropy dis-
 1087 tribution, $T(\mathbf{x}, \mathbf{z})$ is comprised of both these first and second moments of the hub neuron frequency

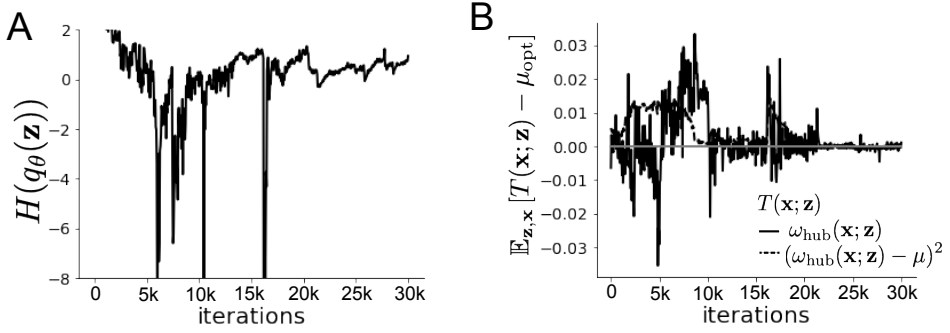


Figure 9: (STG1): EPI optimization of the STG model producing network syncing. **A.** Entropy throughout optimization. **B.** The emergent property statistic means and variances converge to their constraints at 25,000 iterations following the fifth augmented Lagrangian epoch.

1088 (as in Equations 27 and 28)

$$T(\mathbf{x}; \mathbf{z}) = \begin{bmatrix} \omega_{\text{hub}}(\mathbf{x}; \mathbf{z}) \\ (\omega_{\text{hub}}(\mathbf{x}; \mathbf{z}) - 0.55)^2 \end{bmatrix}, \quad (58)$$

$$\boldsymbol{\mu}_{\text{opt}} = \begin{bmatrix} 0.55 \\ 0.025^2 \end{bmatrix}. \quad (59)$$

1090 Throughout optimization, the augmented Lagrangian parameters η and c , were updated after each
1091 epoch of 5,000 iterations (see Section 5.1.3). The optimization converged after five epochs (Fig. S4).

1092 For EPI in Fig 1E, we used a real NVP architecture with three Real NVP coupling layers and two-
1093 layer neural networks of 25 units per layer. The normalizing flow architecture mapped $z_0 \sim \mathcal{N}(\mathbf{0}, I)$
1094 to a support of $\mathbf{z} = [g_{\text{el}}, g_{\text{synA}}] \in [4, 8] \times [0.01, 4]$, initialized to a gaussian approximation of samples
1095 returned by a preliminary ABC search. We did not include $g_{\text{synA}} < 0.01$, for numerical stability.
1096 EPI optimization was run using 5 different random seeds for architecture initialization $\boldsymbol{\theta}$ with an
1097 augmented Lagrangian coefficient of $c_0 = 10^5$, a batch size $n = 400$, and $\beta = 2$. The distribution
1098 shown is that of the architecture converging with criteria $N_{\text{test}} = 100$ at greatest entropy across
1099 random seeds.

1100 We calculated the Hessian at the mode of the inferred EPI distribution. The Hessian of a probability
1101 model is the second order gradient of the log probability density $\log q_{\boldsymbol{\theta}}(\mathbf{z})$ with respect to the
1102 parameters \mathbf{z} : $\frac{\partial^2 \log q_{\boldsymbol{\theta}}(\mathbf{z})}{\partial \mathbf{z} \partial \mathbf{z}^T}$. With EPI, we can examine the Hessian, which is analytically available
1103 throughout distribution, to indicate the dimensions of parameter space that are sensitive (strongly
1104 negative eigenvalue), and which are degenerate (low magnitude eigenvalue) with respect to the

emergent property produced. In Figure 1D, the eigenvectors of the Hessian v_1 (solid) and v_2 (dashed) are shown evaluated at the mode of the distribution. The length of the arrows is inversely proportional to the square root of absolute value of their eigenvalues $\lambda_1 = -10.7$ and $\lambda_2 = -3.22$. Since the Hessian eigenvectors have sign degeneracy, the visualized directions in 2-D parameter space are chosen arbitrarily.

5.2.2 Scaling EPI for stable amplification in RNNs

We examined the scaling properties of EPI by learning connectivities of RNNs of increasing size that exhibit stable amplification. Rank-2 RNN connectivity was modeled as $W = UV^\top$, where $U = [\mathbf{u}_1 \ \mathbf{u}_2] + g\chi^{(W)}$, $V = [\mathbf{v}_1 \ \mathbf{v}_2] + g\chi^{(V)}$, and $\chi_{i,j}^{(W)}, \chi_{i,j}^{(V)} \sim \mathcal{N}(0, 1)$. This RNN model has dynamics

$$\tau \dot{\mathbf{x}} = -\mathbf{x} + W\mathbf{x}. \quad (60)$$

In this analysis, we inferred connectivity parameterizations $\mathbf{z} = [\mathbf{u}_1^\top, \mathbf{u}_2^\top, \mathbf{v}_1^\top, \mathbf{v}_2^\top]^\top \in [-1, 1]^{(4N)}$ that produced stable amplification using EPI, SMC-ABC [41], and SNPE [43] (see Section Related Methods).

For this RNN model to be stable, all real eigenvalues of W must be less than 1: $\text{real}(\lambda_1) < 1$, where λ_1 denotes the greatest real eigenvalue of W . For a stable RNN to amplify at least one input pattern, the symmetric connectivity $W^s = \frac{W+W^\top}{2}$ must have an eigenvalue greater than 1: $\lambda_1^s > 1$, where λ^s is the maximum eigenvalue of W^s . These two conditions are necessary and sufficient for stable amplification in RNNs [61]. We defined the emergent property of stable amplification with means of these eigenvalues (0.5 and 1.5, respectively) that satisfy these conditions. To complete the emergent property definition, we chose variances (0.25^2) about those means such that samples rarely violate the eigenvalue constraints. In terms of the EPI optimization variables, this is written as

$$T(\mathbf{x}; \mathbf{z}) = \begin{bmatrix} \text{real}(\lambda_1)(\mathbf{x}; \mathbf{z}) \\ \lambda_1^s(\mathbf{x}; \mathbf{z}) \\ (\text{real}(\lambda_1)(\mathbf{x}; \mathbf{z}) - 0.5)^2 \\ (\lambda_1^s(\mathbf{x}; \mathbf{z}) - 1.5)^2 \end{bmatrix}, \quad (61)$$

$$\boldsymbol{\mu}_{\text{opt}} = \begin{bmatrix} 0.5 \\ 1.5 \\ 0.25^2 \\ 0.25^2 \end{bmatrix}. \quad (62)$$

1128 Gradients of maximum eigenvalues of Hermitian matrices like W^s are available with modern auto-
 1129 automatic differentiation tools. To differentiate through the $\text{real}(\lambda_1)$, we solved the following equation
 1130 for eigenvalues of rank-2 matrices using the rank reduced matrix $W^r = V^\top U$

$$\lambda_{\pm} = \frac{\text{Tr}(W^r) \pm \sqrt{\text{Tr}(W^r)^2 - 4\text{Det}(W^r)}}{2}. \quad (63)$$

1131 For EPI in Fig. 2, we used a real NVP architecture with three coupling layers of affine transfor-
 1132 mations parameterized by two-layer neural networks of 100 units per layer. The initial distribution
 1133 was a standard isotropic gaussian $z_0 \sim \mathcal{N}(\mathbf{0}, I)$ mapped to the support of $\mathbf{z}_i \in [-1, 1]$. We used
 1134 an augmented Lagrangian coefficient of $c_0 = 10^3$, a batch size $n = 200$, $\beta = 4$, and chose to use
 1135 500 iterations per augmented Lagrangian epoch and emergent property constraint convergence was
 1136 evaluated at $N_{\text{test}} = 200$ (Fig. 2B blue line, and Fig. 2C-D blue).

1137 We compared EPI to two alternative likelihood-free inference (LFI) techniques, since the likelihood
 1138 of these eigenvalues given \mathbf{z} is not available. Approximate Bayesian computation (ABC) [77] is a
 1139 rejection sampling technique for obtaining sets of parameters \mathbf{z} that produce activity \mathbf{x} close to some
 1140 observed data \mathbf{x}_0 . Sequential Monte Carlo approximate Bayesian computation (SMC-ABC) is the
 1141 state-of-the-art ABC method, which leverages SMC techniques to improve sampling speed. We ran
 1142 SMC-ABC with the pyABC package [101] to infer RNNs with stable amplification: connectivities
 1143 having eigenvalues within an ϵ -defined l_2 distance of

$$x_0 = \begin{bmatrix} \text{real}(\lambda_1) \\ \lambda_1^s \end{bmatrix} = \begin{bmatrix} 0.5 \\ 1.5 \end{bmatrix}. \quad (64)$$

1144 SMC-ABC was run with a uniform prior over $\mathbf{z} \in [-1, 1]^{(4N)}$, a population size of 1,000 particles
 1145 with simulations parallelized over 32 cores, and a multivariate normal transition model.

1146 SNPE, the next LFI approach in our comparison, is far more similar to EPI. Like EPI, SNPE
 1147 treats parameters in mechanistic models with deep probability distributions, yet the two learning
 1148 algorithms are categorically different. SNPE uses a two-network architecture to approximate the
 1149 posterior distribution of the model conditioned on observed data \mathbf{x}_0 . The amortizing network maps
 1150 observations \mathbf{x}_i to the parameters of the deep probability distribution. The weights and biases of the
 1151 parameter network are optimized by sequentially augmenting the training data with additional pairs
 1152 $(\mathbf{z}_i, \mathbf{x}_i)$ based on the most recent posterior approximation. This sequential procedure is important
 1153 to get training data \mathbf{z}_i to be closer to the true posterior, and \mathbf{x}_i to be closer to the observed data.
 1154 For the deep probability distribution architecture, we chose a masked autoregressive flow with affine
 1155 couplings (the default choice), three transforms, 50 hidden units, and a normalizing flow mapping

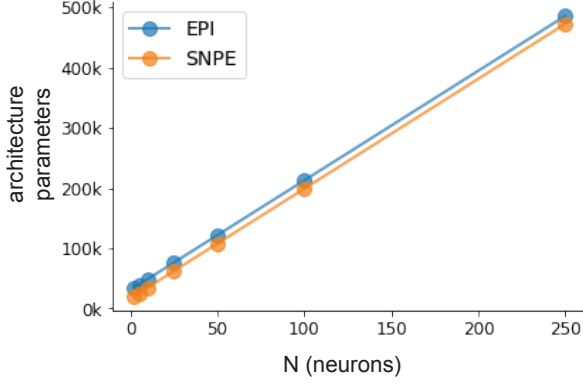


Figure 10: (RNN1): Number of parameters in deep probability distribution architectures of EPI (blue) and SNPE (orange) by RNN size (N).

1156 to the support as in EPI. This architectural choice closely tracked the size of the architecture used
 1157 by EPI (Fig. 10). As in SMC-ABC, we ran SNPE with $\mathbf{x}_0 = \mu$. All SNPE optimizations were
 1158 run for a limit of 1.5 days on a Tesla V100 GPU, or until two consecutive rounds resulted in a
 1159 validation log probability lower than the maximum observed for that random seed.

1160 To clarify the difference in objectives of EPI and SNPE, we show their results on RNN models
 1161 with different numbers of neurons N and random strength g . The parameters inferred by EPI
 1162 consistently produces the same mean and variance of $\text{real}(\lambda_1)$ and λ_1^s , while those inferred by
 1163 SNPE change according to the model definition (Fig. 11A). For $N = 2$ and $g = 0.01$, the SNPE
 1164 posterior has greater concentration in eigenvalues around \mathbf{x}_0 than at $g = 0.1$, where the model has
 1165 greater randomness (Fig. 11B top, orange). At both levels of g when $N = 2$, the posterior of SNPE
 1166 has lower entropy than EPI at convergence (Fig. 11B top). However at $N = 10$, SNPE results in
 1167 a predictive distribution of more widely dispersed eigenvalues (Fig. 11A bottom), and an inferred
 1168 posterior with greater entropy than EPI (Fig. 11B bottom). We highlight these differences not
 1169 to focus on an insightful trend, but to emphasize that these methods optimize different objectives
 1170 with different implications.

1171 Note that SNPE converges when it's validation log probability has saturated after several rounds
 1172 of optimization (Fig. 11C), and that EPI converges after several epochs of its own optimization
 1173 to enforce the emergent property constraints (Fig. 11D blue). Importantly, as SNPE optimizes
 1174 its posterior approximation, the predictive means change, and at convergence may be different
 1175 than \mathbf{x}_0 (Fig. 11D orange, left). It is sensible to assume that predictions of a well-approximated
 1176 SNPE posterior should closely reflect the data on average (especially given a uniform prior and

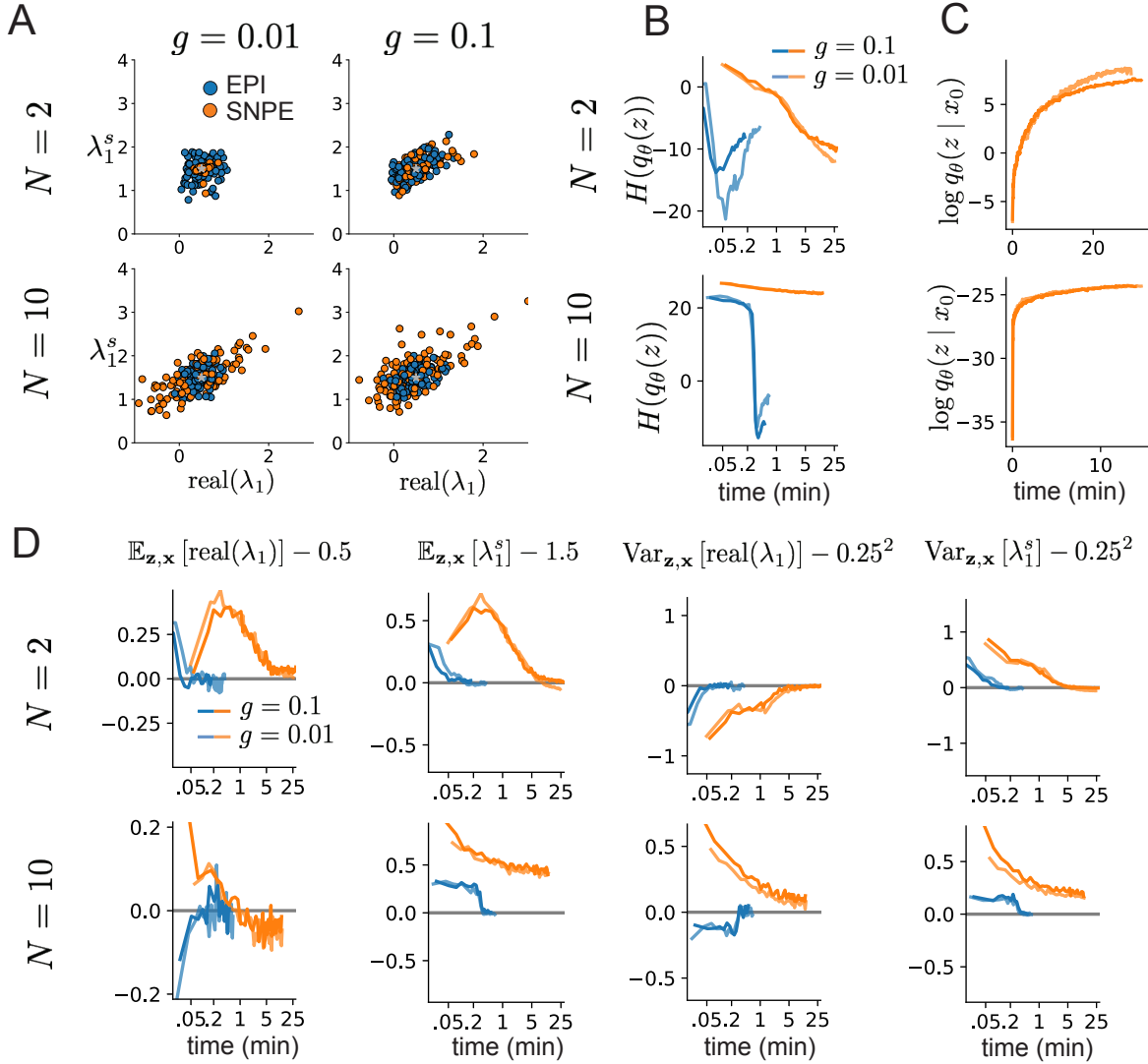


Figure 11: (RNN2): Model characteristics affect predictions of posteriors inferred by SNPE, while predictions of parameters inferred by EPI remain fixed. **A.** Predictive distribution of EPI (blue) and SNPE (orange) inferred connectivity of RNNs exhibiting stable amplification with $N = 2$ (top), $N = 10$ (bottom), $g = 0.01$ (left), and $g = 0.1$ (right). **B.** Entropy of parameter distribution approximations throughout optimization with $N = 2$ (top), $N = 10$ (bottom), $g = 0.1$ (dark shade), and $g = 0.01$ (light shade). **C.** Validation log probabilities throughout SNPE optimization. Same conventions as B. **D.** Adherence to EPI constraints. Same conventions as B.

1177 a low degree of stochasticity), however this is not a given. Furthermore, no aspect of the SNPE
1178 optimization controls the variance of the predictions (Fig. 11D orange, right).

1179 To compare the efficiency of these algorithms for inferring RNN connectivity distributions producing
1180 stable amplification, we develop a convergence criteria that can be used across methods. While EPI
1181 has its own hypothesis testing convergence criteria for the emergent property, it would not make
1182 sense to use this criteria on SNPE and SMC-ABC which do not constrain the means and variances
1183 of their predictions. Instead, we consider EPI and SNPE to have converged after completing its
1184 most recent optimization epoch (EPI) or round (SNPE) in which the distance

$$d(q_\theta(z)) = |\mathbb{E}_{\mathbf{z}, \mathbf{x}} [f(\mathbf{x}; \mathbf{z})] - \boldsymbol{\mu}|_2 \quad (65)$$

1185 is less than 0.5. We consider SMC-ABC to have converged once the population produces samples
1186 within the $\epsilon = 0.5$ ball ensuring stable amplification.

1187 When assessing the scalability of SNPE, it is important to check that alternative hyperparameter-
1188 izations could not yield better performance. Key hyperparameters of the SNPE optimization are
1189 the number of simulations per round n_{round} , the number of atoms used in the atomic proposals of
1190 the SNPE-C algorithm [102], and the batch size n . To match EPI, we used a batch size of $n = 200$
1191 for $N \leq 25$, however we found $n = 1,000$ to be helpful for SNPE in higher dimensions. While
1192 $n_{\text{round}} = 1,000$ yielded SNPE convergence for $N \leq 25$, we found that a substantial increase to
1193 $n_{\text{round}} = 25,000$ yielded more consistent convergence at $N = 50$ (Fig. 12A). By increasing n_{round} ,
1194 we also necessarily increase the duration of each round. At $N = 100$, we tried two hyperparameter
1195 modifications. As suggested in [102], we increased n_{atom} by an order of magnitude to improve
1196 gradient quality, but this had little effect on the optimization (much overlap between same random
1197 seeds) (Fig. 12B). Finally, we increased n_{round} by an order of magnitude, which yielded convergence
1198 in one case, but no others. We found no way to improve the convergence rate of SNPE without
1199 making more aggressive hyperparameter choices requiring high numbers of simulations.

1200 In Figure 2C-D, we show samples from the random seed resulting in emergent property convergence
1201 at greatest entropy (EPI), the random seed resulting in greatest validation log probability (SNPE),
1202 and the result of all converged random seeds (SMC).

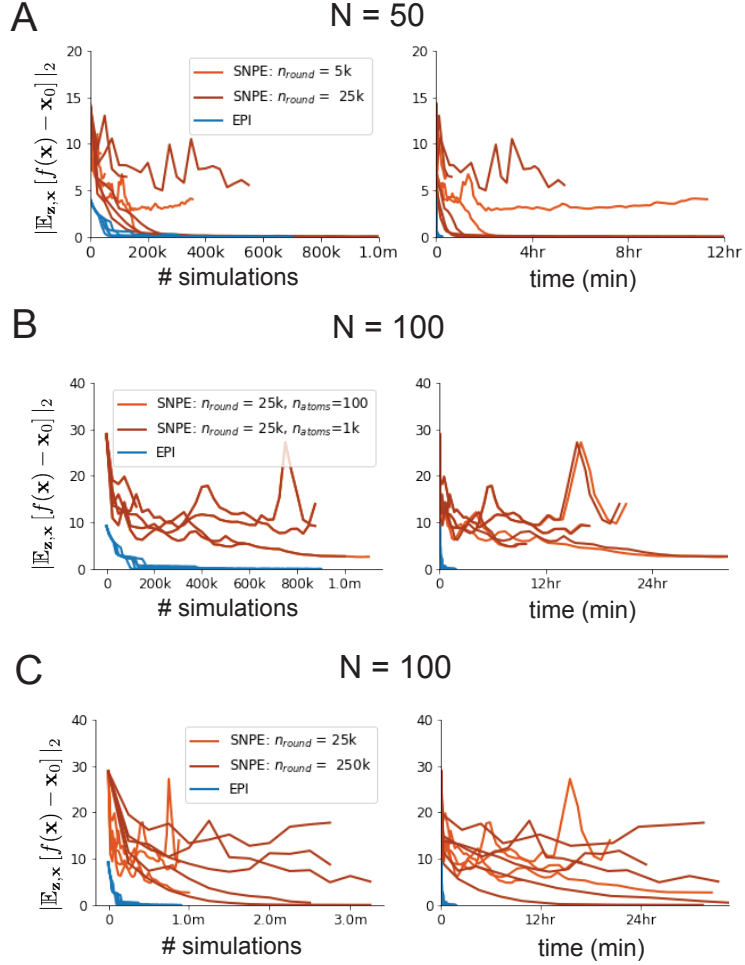


Figure 12: (RNN3): SNPE convergence was enabled by increasing n_{round} , not n_{atom} . **A.** Difference of mean predictions \mathbf{x}_0 throughout optimization at $N = 50$ with by simulation count (left) and wall time (right) of SNPE with $n_{\text{round}} = 5,000$ (light orange), SNPE with $n_{\text{round}} = 25,000$ (dark orange), and EPI (blue). Each line shows an individual random seed. **B.** Same conventions as A at $N = 100$ of SNPE with $n_{\text{atom}} = 100$ (light orange) and $n_{\text{atom}} = 1,000$ (dark orange). **C.** Same conventions as A at $N = 100$ of SNPE with $n_{\text{round}} = 25,000$ (light orange) and $n_{\text{round}} = 250,000$ (dark orange).

1203 **5.2.3 Primary visual cortex**

1204 In the stochastic stabilized supralinear network [75], population rate responses \mathbf{x} to input \mathbf{h} , recur-
 1205 rent input $W\mathbf{x}$ and slow noise ϵ are governed by

$$\tau \frac{d\mathbf{x}}{dt} = -\mathbf{x} + \phi(W\mathbf{x} + \mathbf{h} + \epsilon), \quad (66)$$

1206 where the noise is an Ornstein-Uhlenbeck process $\epsilon \sim OU(\tau_{\text{noise}}, \sigma)$

$$\tau_{\text{noise}} d\epsilon_\alpha = -\epsilon_\alpha dt + \sqrt{2\tau_{\text{noise}}} \tilde{\sigma}_\alpha dB \quad (67)$$

1207 with $\tau_{\text{noise}} = 5\text{ms} > \tau = 1\text{ms}$. The noisy process is parameterized as

$$\tilde{\sigma}_\alpha = \sigma_\alpha \sqrt{1 + \frac{\tau}{\tau_{\text{noise}}}}, \quad (68)$$

1208 so that σ parameterizes the variance of the noisy input in the absence of recurrent connectivity
 1209 ($W = \mathbf{0}$). As contrast increases, input to the E- and P-populations increases relative to a baseline
 1210 input $\mathbf{h} = \mathbf{h}_b + c\mathbf{h}_c$. Connectivity (W_{fit}) and input ($\mathbf{h}_{b,\text{fit}}$ and $\mathbf{h}_{c,\text{fit}}$) parameters were fit using the
 1211 deterministic V1 circuit model [55]

$$W_{\text{fit}} = \begin{bmatrix} W_{EE} & W_{EP} & W_{ES} & W_{EV} \\ W_{PE} & W_{PP} & W_{PS} & W_{PV} \\ W_{SE} & W_{SP} & W_{SS} & W_{SV} \\ W_{VE} & W_{VP} & W_{VS} & W_{VV} \end{bmatrix} = \begin{bmatrix} 2.18 & -1.19 & -.594 & -.229 \\ 1.66 & -.651 & -.680 & -.242 \\ .895 & -5.22 \times 10^{-3} & -1.51 \times 10^{-4} & -.761 \\ 3.34 & -2.31 & -.254 & -2.52 \times 10^{-4} \end{bmatrix}, \quad (69)$$

$$\mathbf{h}_{b,\text{fit}} = \begin{bmatrix} .416 \\ .429 \\ .491 \\ .486 \end{bmatrix}, \quad (70)$$

1212 and

$$\mathbf{h}_{c,\text{fit}} = \begin{bmatrix} .359 \\ .403 \\ 0 \\ 0 \end{bmatrix}. \quad (71)$$

1213 To obtain rates on a realistic scale (100-fold greater), we map these fitted parameters to an equiv-
 1214 alence class

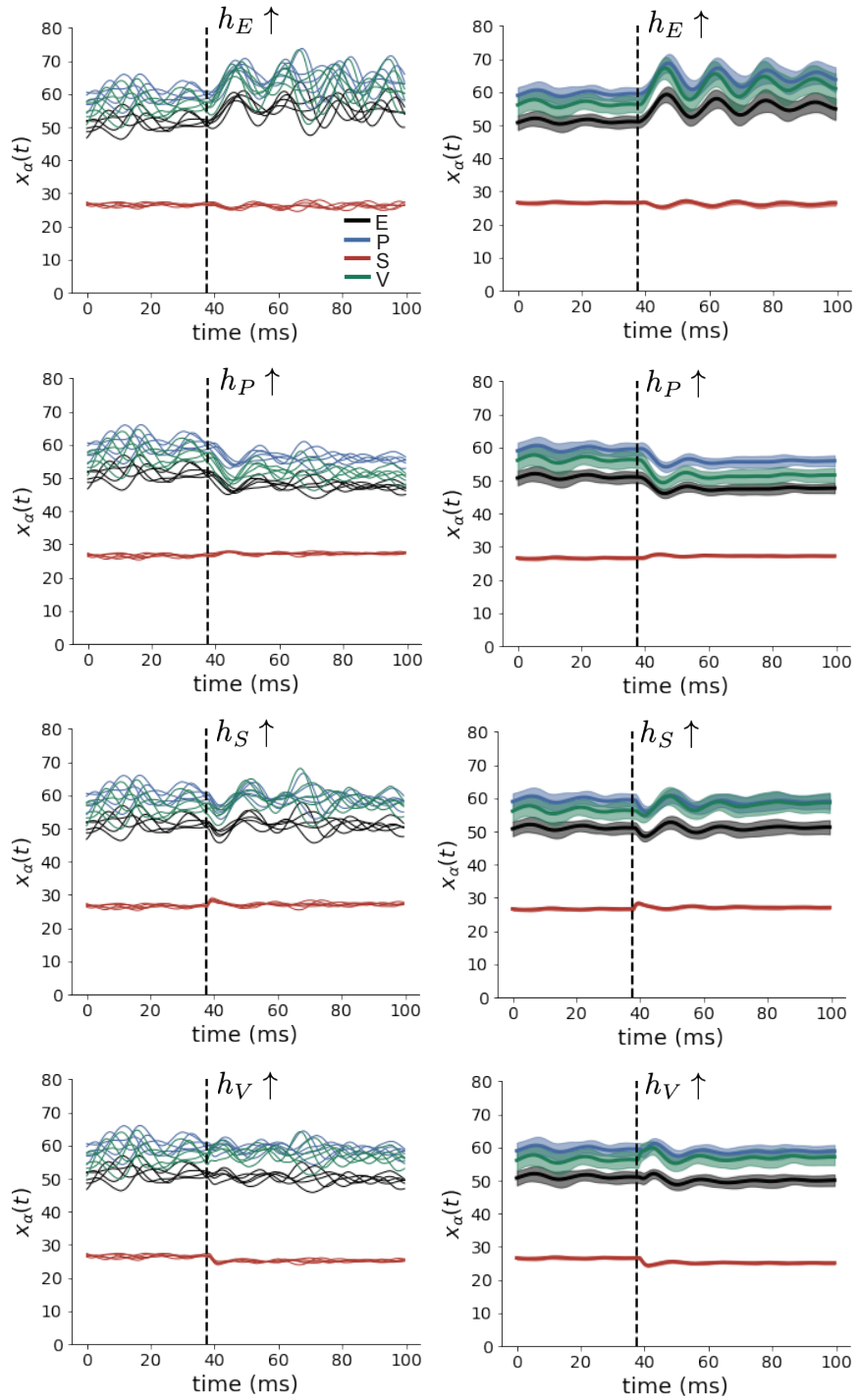


Figure 13: (V1 1) (Left) Simulations for small increases in neuron-type population input. Input magnitudes are chosen so that effect is salient (0.002 for E and P, but 0.02 for S and V). (Right) Average (solid) and standard deviation (shaded) of stochastic fluctuations of responses.

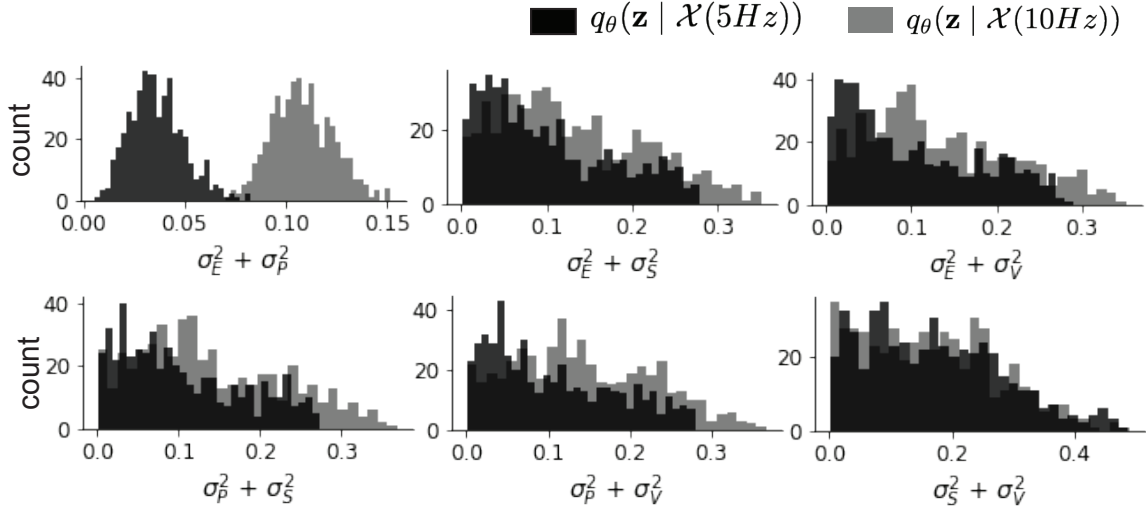


Figure 14: (V1 2) EPI predictive distributions of the sum of squares of each pair of noise parameters.

$$W = \begin{bmatrix} W_{EE} & W_{EP} & W_{ES} & W_{EV} \\ W_{PE} & W_{PP} & W_{PS} & W_{PV} \\ W_{SE} & W_{SP} & W_{SS} & W_{SV} \\ W_{VE} & W_{VP} & W_{VS} & W_{VV} \end{bmatrix} = \begin{bmatrix} .218 & -.119 & -.0594 & -.0229 \\ .166 & -.0651 & -.068 & -.0242 \\ .0895 & -5.22 \times 10^{-4} & -1.51 \times 10^{-5} & -.0761 \\ .334 & -.231 & -.0254 & -2.52 \times 10^{-5} \end{bmatrix}, \quad (72)$$

$$\mathbf{h}_b = \begin{bmatrix} h_{b,E} \\ h_{b,P} \\ h_{b,S} \\ h_{b,V} \end{bmatrix} = \begin{bmatrix} 4.16 \\ 4.29 \\ 4.91 \\ 4.86 \end{bmatrix}, \quad (73)$$

1215 and

$$\mathbf{h}_c = \begin{bmatrix} h_{c,E} \\ h_{c,P} \\ h_{c,S} \\ h_{c,V} \end{bmatrix} = \begin{bmatrix} 3.59 \\ 4.03 \\ 0 \\ 0 \end{bmatrix}. \quad (74)$$

1216 Circuit responses are simulated using $T = 200$ time steps at $dt = 0.5\text{ms}$ from an initial condition
 1217 drawn from $\mathbf{x}(0) \sim U[10 \text{ Hz}, 25 \text{ Hz}]$. Standard deviation of the E-population $s_E(\mathbf{x}; \mathbf{z})$ is calculated
 1218 as the square root of the temporal variance from $t_{ss} = 75\text{ms}$ to $Tdt = 100\text{ms}$ averaged over 100

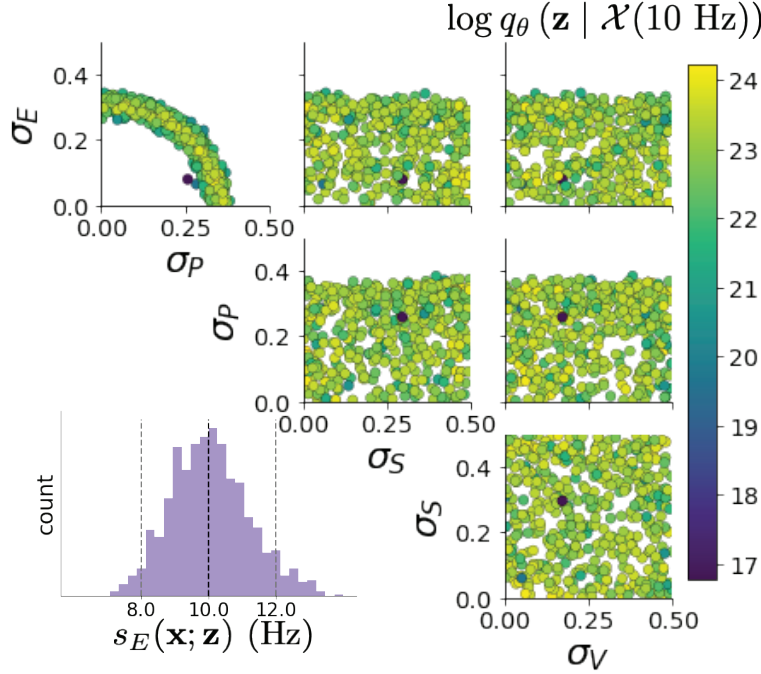


Figure 15: (V1 3) EPI inferred distribution for $\mathcal{X}(10 \text{ Hz})$.

1219 independent trials.

$$s_E(\mathbf{x}; \mathbf{z}) = \mathbb{E}_x \left[\sqrt{\mathbb{E}_{t > t_{ss}} \left[(x_E(t) - \mathbb{E}_{t > t_{ss}} [x_E(t)])^2 \right]} \right] \quad (75)$$

1220 For EPI in Fig 3D-E, we used a real NVP architecture with three Real NVP coupling layers
 1221 and two-layer neural networks of 50 units per layer. The normalizing flow architecture mapped
 1222 $z_0 \sim \mathcal{N}(\mathbf{0}, I)$ to a support of $\mathbf{z} = [\sigma_E, \sigma_P, \sigma_S, \sigma_V] \in [0.0, 0.5]^4$. EPI optimization was run using three
 1223 different random seeds for architecture initialization θ with an augmented Lagrangian coefficient of
 1224 $c_0 = 10^{-1}$, a batch size $n = 100$, and $\beta = 2$. The distributions shown are those of the architectures
 1225 converging with criteria $N_{\text{test}} = 100$ at greatest entropy across random seeds.

1226 In Fig. 3E, we visualize the modes of $q_\theta(\mathbf{z} | \mathcal{X})$ throughout the σ_E - σ_P marginal. Specifically, we
 1227 calculated

$$\begin{aligned} \mathbf{z}^*(\sigma_{P,\text{fixed}}) &= \underset{\mathbf{z}}{\operatorname{argmax}} \log q_\theta(\mathbf{z} | \mathcal{X}) \\ \text{s.t. } \sigma_P &= \sigma_{P,\text{fixed}} \end{aligned} \quad (76)$$

1228 At each mode \mathbf{z}^* , we calculated the Hessian and visualized the sensitivity dimension in the direction
 1229 of positive σ_E .

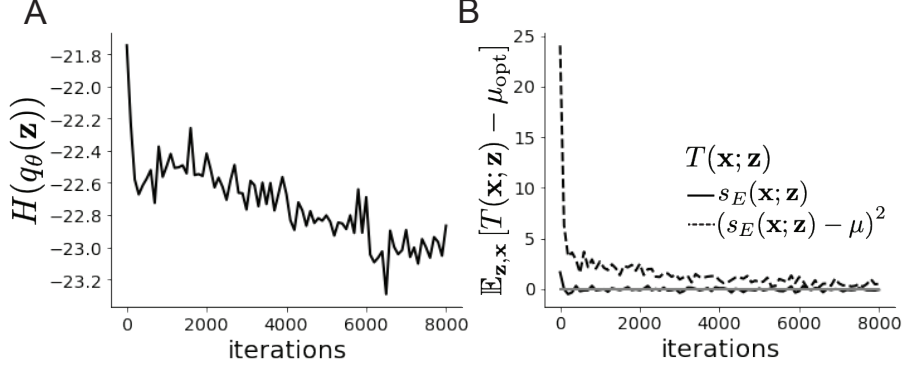


Figure 16: (V1 4) Optimization for V1

1230 **5.2.4 Primary visual cortex: challenges to analysis**

1231 TODO Agostina and I are putting this together now.

1232 **5.2.5 Superior colliculus**

1233 The ability to switch between two separate tasks throughout randomly interleaved trials, or “rapid
1234 task switching,” has been studied in rats, and midbrain superior colliculus (SC) has been shown to
1235 play an important role in this computation [76]. Neural recordings in SC exhibited two populations of
1236 neurons that simultaneously represented both task context (Pro or Anti) and motor response (con-
1237 tralateral or ipsilateral to the recorded side), which led to the distinction of two functional classes:
1238 the Pro/Contra and Anti/Ipsi neurons [56]. Given this evidence, Duan et al. proposed a model
1239 with four functionally-defined neuron-type populations: two in each hemisphere corresponding to
1240 the Pro/Contra and Anti/Ipsi populations. We study how the connectivity of this neural circuit
1241 governs rapid task switching ability.

1242 The four populations of this model are denoted as left Pro (LP), left Anti (LA), right Pro (RP)
1243 and right Anti (RA). Each unit has an activity (x_α) and internal variable (u_α) related by

$$x_\alpha = \phi(u_\alpha) = \left(\frac{1}{2} \tanh \left(\frac{u_\alpha - a}{b} \right) + \frac{1}{2} \right), \quad (77)$$

1244 where $\alpha \in \{LP, LA, RA, RP\}$, $a = 0.05$ and $b = 0.5$ control the position and shape of the nonlin-

earily. We order the neural populations of x and u in the following manner

$$\mathbf{x} = \begin{bmatrix} x_{LP} \\ x_{LA} \\ x_{RP} \\ x_{RA} \end{bmatrix} \quad \mathbf{u} = \begin{bmatrix} u_{LP} \\ u_{LA} \\ u_{RP} \\ u_{RA} \end{bmatrix}, \quad (78)$$

which evolve according to

$$\tau \frac{d\mathbf{u}}{dt} = -\mathbf{u} + W\mathbf{x} + \mathbf{h} + d\mathbf{B}. \quad (79)$$

with time constant $\tau = 0.09s$, step size 24ms and Gaussian noise $d\mathbf{B}$ of variance 0.2^2 . These hyperparameter values are motivated by modeling choices and results from [56].

The weight matrix has 4 parameters for self sW , vertical vW , horizontal hW , and diagonal dW connections:

$$W = \begin{bmatrix} sW & vW & hW & dW \\ vW & sW & dW & hW \\ hW & dW & sW & vW \\ dW & hW & vW & sW \end{bmatrix}. \quad (80)$$

We study the role of parameters $\mathbf{z} = [sW, vW, hW, dW]^\top$ in rapid task switching.

The circuit receives four different inputs throughout each trial, which has a total length of 1.8s.

$$\mathbf{h} = \mathbf{h}_{\text{constant}} + \mathbf{h}_{\text{P,bias}} + \mathbf{h}_{\text{rule}} + \mathbf{h}_{\text{choice-period}} + \mathbf{h}_{\text{light}}. \quad (81)$$

There is a constant input to every population,

$$\mathbf{h}_{\text{constant}} = I_{\text{constant}}[1, 1, 1, 1]^\top, \quad (82)$$

a bias to the Pro populations

$$\mathbf{h}_{\text{P,bias}} = I_{\text{P,bias}}[1, 0, 1, 0]^\top, \quad (83)$$

rule-based input depending on the condition

$$\mathbf{h}_{\text{P,rule}}(t) = \begin{cases} I_{\text{P,rule}}[1, 0, 1, 0]^\top, & \text{if } t \leq 1.2s \\ 0, & \text{otherwise} \end{cases} \quad (84)$$

$$\mathbf{h}_{\text{A,rule}}(t) = \begin{cases} I_{\text{A,rule}}[0, 1, 0, 1]^\top, & \text{if } t \leq 1.2s \\ 0, & \text{otherwise} \end{cases}, \quad (85)$$

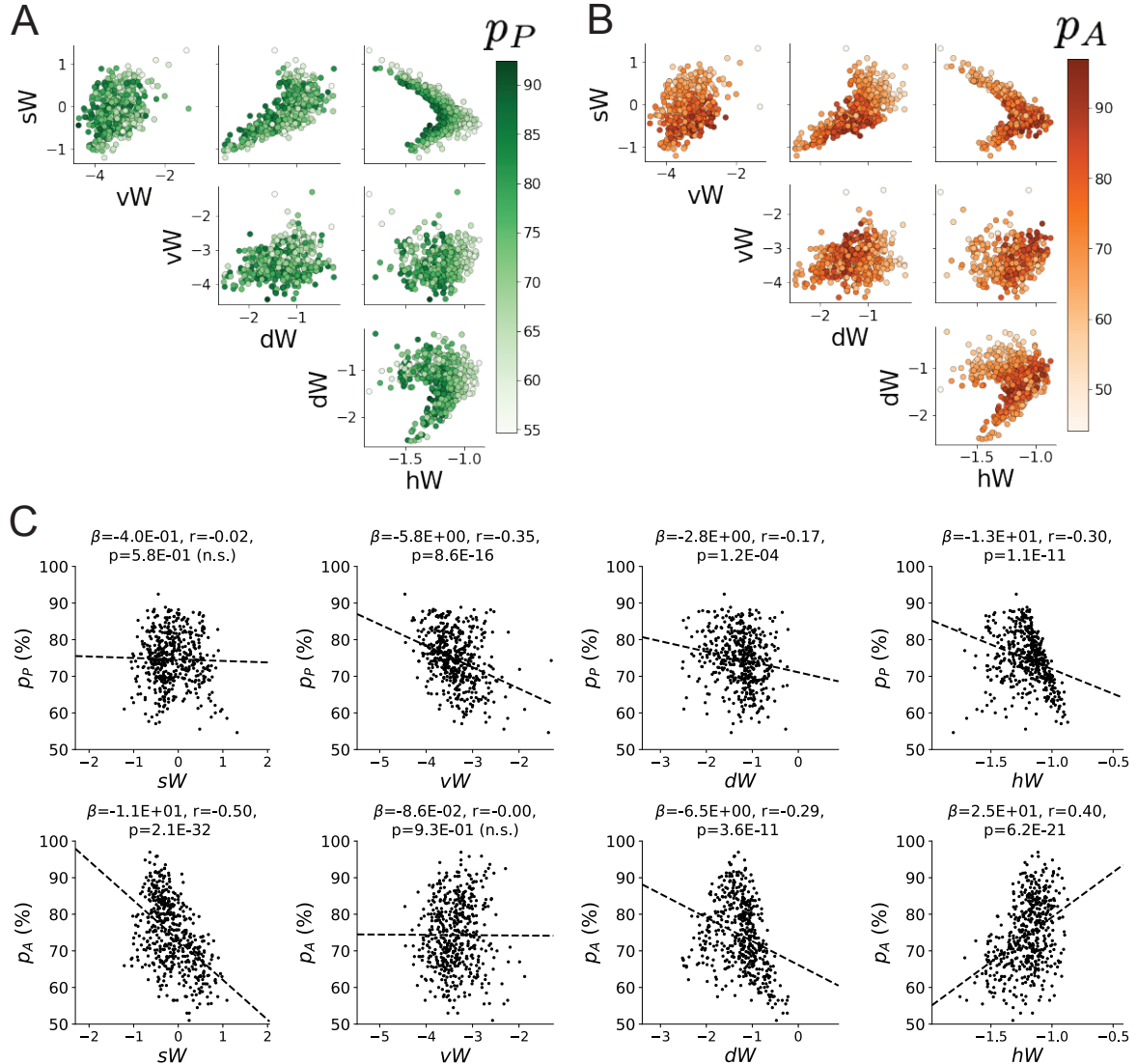


Figure 17: (SC1): **A.** Same pairplot as Fig. 4C colored by Pro task accuracy. **B.** Same as A colored by Anti task accuracy. **C.** Connectivity parameters of EPI distributions versus task accuracies. β is slope coefficient of linear regression, r is correlation, and p is the two-tailed p-value.

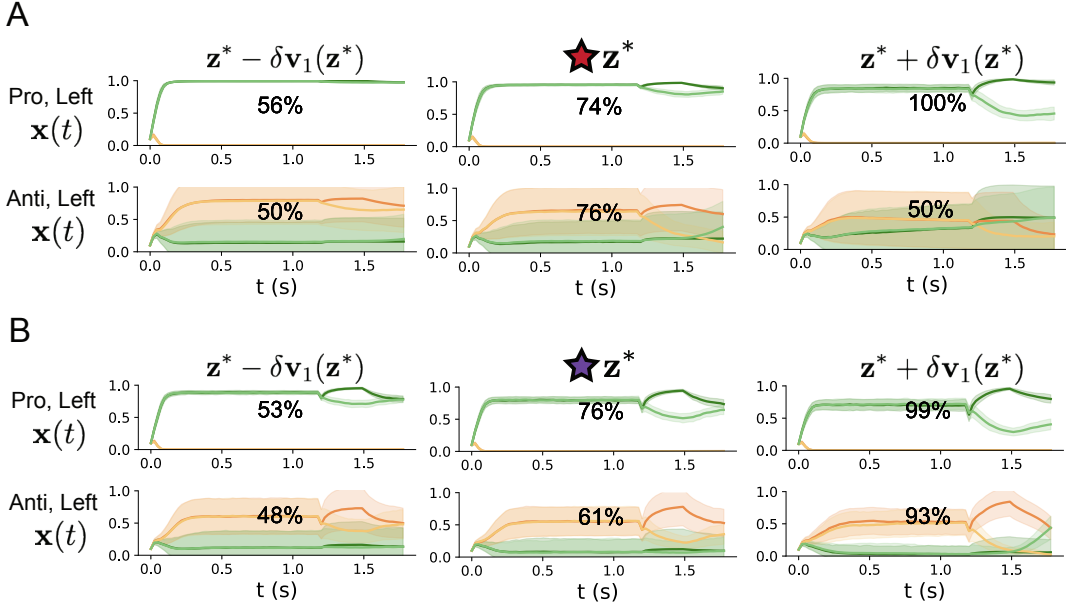


Figure 18: (SC2): **A.** Simulations in network regime 1 ($hW_{\text{fixed}} = -1.2$) (center) with simulations given connectivity perturbations in the negative direction of the sensitivity vector \mathbf{v}_1 (left) and positive direction (right). **B.** Same as A for network regime 2.

1257 a choice-period input

$$\mathbf{h}_{\text{choice}}(t) = \begin{cases} I_{\text{choice}}[1, 1, 1, 1]^{\top}, & \text{if } t > 1.2s \\ 0, & \text{otherwise} \end{cases}, \quad (86)$$

1258 and an input to the right or left-side depending on where the light stimulus is delivered

$$\mathbf{h}_{\text{light}}(t) = \begin{cases} I_{\text{light}}[1, 1, 0, 0]^{\top}, & \text{if } 1.2s < t < 1.5s \text{ and Left} \\ I_{\text{light}}[0, 0, 1, 1]^{\top}, & \text{if } 1.2s < t < 1.5s \text{ and Right} \\ 0, & \text{otherwise} \end{cases}. \quad (87)$$

1259 The input parameterization was fixed to $I_{\text{constant}} = 0.75$, $I_{\text{P,bias}} = 0.5$, $I_{\text{P,rule}} = 0.6$, $I_{\text{A,rule}} = 0.6$,

1260 $I_{\text{choice}} = 0.25$, and $I_{\text{light}} = 0.5$.

1261 The accuracies of each task p_P and p_A are calculated as

$$p_P(\mathbf{x}; \mathbf{z}) = \mathbb{E}_{\mathbf{x}} [\Theta[x_{LP}(t = 1.8s) - x_{RP}(t = 1.8s)]] \quad (88)$$

1262 and

$$p_A(\mathbf{x}; \mathbf{z}) = \mathbb{E}_{\mathbf{x}} [\Theta[x_{RP}(t = 1.8s) - x_{LP}(t = 1.8s)]] \quad (89)$$

1263 given that the stimulus is on the left side, where Θ is the Heaviside step function, and the accuracy

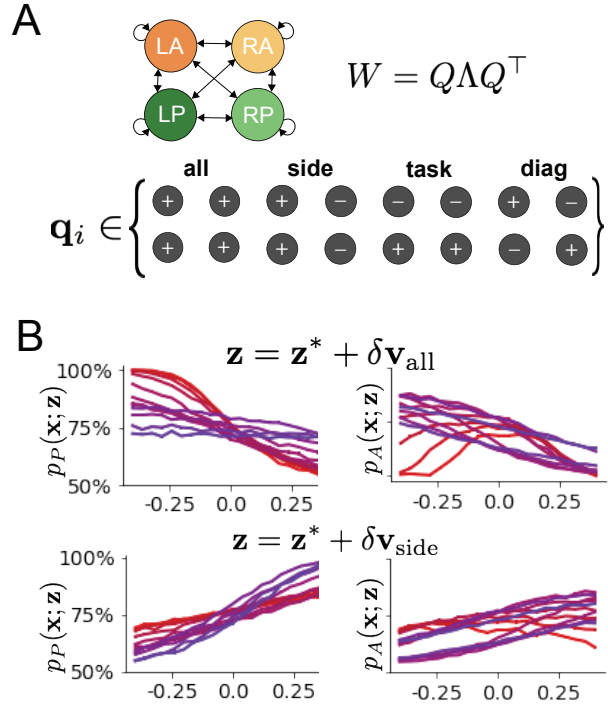


Figure 19: (SC3): **A.** Invariant eigenvectors of connectivity matrix W . **B.** Accuracies for connectivity perturbations for increasing λ_{all} and λ_{side} (rest shown in Fig. 4D).

₁₂₆₄ is averaged over 200 independent trials. The Heaviside step function is approximated as

$$\Theta(\mathbf{x}) = \text{sigmoid}(\beta \mathbf{x}), \quad (90)$$

₁₂₆₅ where $\beta = 100$.

₁₂₆₆ Writing the EPI distribution as a maximum entropy distribution, $T(\mathbf{x}, \mathbf{z})$ is comprised of both these
₁₂₆₇ first and second moments of the accuracy in each task (as in Equations 27 and 28)

$$T(\mathbf{x}; \mathbf{z}) = \begin{bmatrix} p_P(\mathbf{x}; \mathbf{z}) \\ p_A(\mathbf{x}; \mathbf{z}) \\ (p_P(\mathbf{x}; \mathbf{z}) - 75\%)^2 \\ (p_A(\mathbf{x}; \mathbf{z}) - 75\%)^2 \end{bmatrix}, \quad (91)$$

₁₂₆₈

$$\boldsymbol{\mu}_{\text{opt}} = \begin{bmatrix} 75\% \\ 75\% \\ 7.5\%^2 \\ 7.5\%^2 \end{bmatrix}. \quad (92)$$

₁₂₆₉ Throughout optimization, the augmented Lagrangian parameters η and c , were updated after each

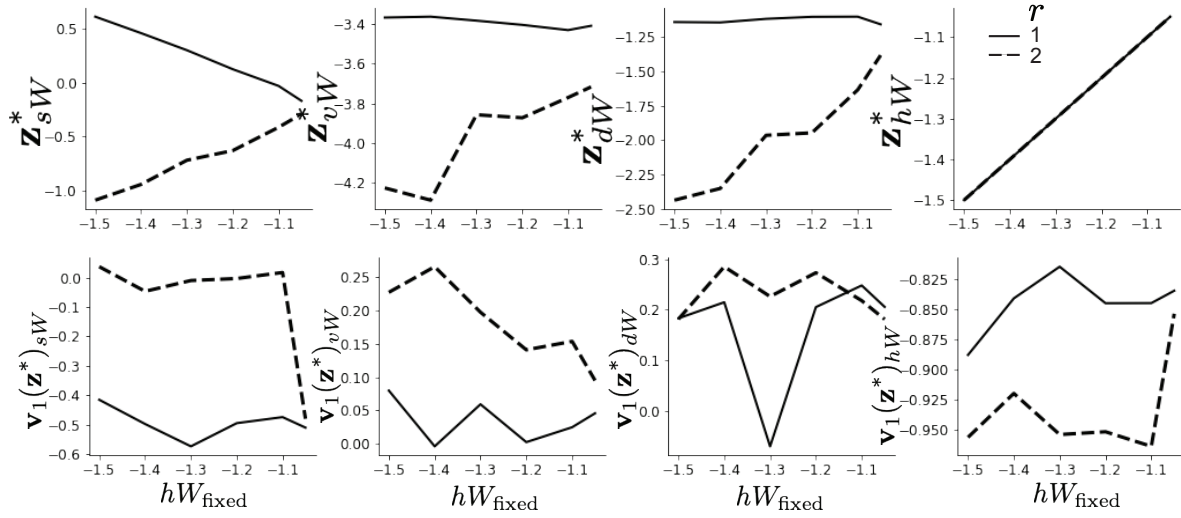


Figure 20: (SC4): **A.** The individual parameters of each mode throughout the two regimes. **B.** The individual sensitivities of parameters of each mode throughout the two regimes.

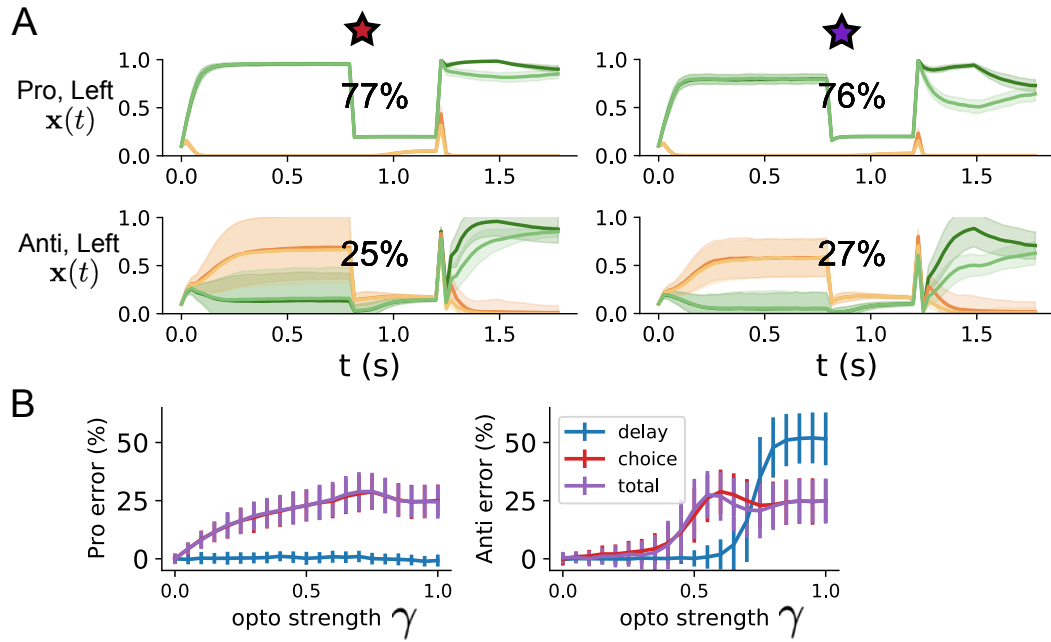


Figure 21: (SC5): **A.** Response of each parameter regime to optogenetic silencing during the delay period. **B.** Error induced by delay period inactivation with increasing optogenetic strength. Means and standard deviations are calculated across the entire EPI distribution.

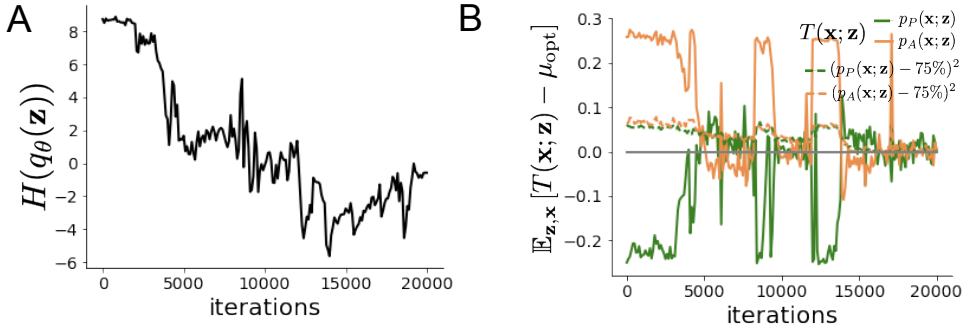


Figure 22: (SC6): **A.** Entropy throughout optimization. **B.** The emergent property statistic means and variances converge to their constraints at 20,000 iterations following the tenth augmented Lagrangian epoch.

epoch of 2,000 iterations (see Section 5.1.3). The optimization converged after ten epochs (Fig. 22).

For EPI in Fig. 4C, we used a real NVP architecture with three coupling layers of affine transformations parameterized by two-layer neural networks of 50 units per layer. The initial distribution was a standard isotropic gaussian $z_0 \sim \mathcal{N}(\mathbf{0}, I)$ mapped to a support of $\mathbf{z}_i \in [-5, 5]$. We used an augmented Lagrangian coefficient of $c_0 = 10^2$, a batch size $n = 100$, and $\beta = 2$. The distribution converged with criteria $N_{\text{test}} = 25$.

The EPI distribution of SC model connectivities producing rapid task switching has interesting structure. Throughout $q_{\theta}(\mathbf{z} \mid \mathcal{X})$, we see that the probability distribution is narrow in hW (Fig. 4C). This suggests that rapid task switching is sensitive to changes in hW , but this is only a single parameter. The local structure of the distribution varies across parameter space, and thus the nature in which parameter combinations affect rapid task switching. From visual inspection, we may hypothesize that there are two distinct regimes, most easily visualized in the sW - hW marginal distribution: one where sW and hW are correlated for greater sW and one where sW and hW are anticorrelated for lesser sW .

We sought two sets of parameters in this distribution representative of each regime, so that we could assess their implications on computation. For fixed values of hW , we hypothesized that there are two modes: one in each regime of greater and lesser sW . To begin, we found one mode for each regime at $hW_{\text{fixed}} = -1.5$ using 200 steps of gradient ascent of the deep probability distribution $q_{\theta}(\mathbf{z} \mid \mathcal{X})$. In regime 1, the initialization had positive sW , and the initialization had negative sW in regime 2, which led to disparate modes (Fig. 20 top). These modes were then used as the initialization to find the next mode at $hW_{\text{fixed}} = -1.4$ and so on. 200 steps of gradient ascent

1292 were always taken, and learning rates of 2.5×10^{-4} and 5×10^{-4} were used for regimes 1 and 2,
 1293 respectively. Each of these modes is denoted $\mathbf{z}^*(hW_{\text{fixed}}, r)$ for regime $r \in \{1, 2\}$.

1294 At each mode, we measure the sensitivity dimension (that of most negative eigenvalue in the Hessian
 1295 of the EPI distribution) $\mathbf{v}_1(\mathbf{z}^*)$. To resolve sign degeneracy in eigenvectors, we chose $\mathbf{v}_1(\mathbf{z}^*)$ to have
 1296 negative element in hW . This tells us what parameter combination rapid task switching is most
 1297 sensitive to at this parameter choice in the regime. We see that while the modes of each regime
 1298 gradually converge to similar connectivities at $hW_{\text{fixed}} = -1.05$ (Fig. 20 top), the sensitivity
 1299 dimensions remain categorically different throughout the two regimes (Fig. 20 bottom). Only at
 1300 $hW_{\text{fixed}} = -1.05$ is there a flip in sensitivity from regime 2 to regime 1 (in $\mathbf{v}_1(\mathbf{z}^*)_{sW}$ and $\mathbf{v}_1(\mathbf{z}^*)_{hW}$).
 1301 There is thus some ambiguity regarding the “regime” of $\mathbf{z}^*(-1.05, 2)$, since the mode is derived
 1302 from an initialization in regime 2, but has sensitivity like regime 1. We can consider this as an
 1303 intermediate transitional region of parameter space between the two regimes. To emphasize this,
 1304 $\mathbf{z}^*(-1.05, 1)$ and $\mathbf{z}^*(-1.05, 2)$ have the same color.

1305 To understand the connectivity mechanisms governing task accuracy, we took the eigendecomposi-
 1306 tion of the symmetric connectivity matrices $W = Q\Lambda Q^{-1}$, which results in the same basis vectors
 1307 \mathbf{q}_i for all W parameterized by \mathbf{z} (Fig. 19A). These basis vectors have intuitive roles in processing for
 1308 this task, and are accordingly named the *all* eigenmode - all neurons co-fluctuate, *side* eigenmode
 1309 - one side dominates the other, *task* eigenmode - the Pro or Anti populations dominate the other,
 1310 and *diag* mode - Pro- and Anti-populations of opposite hemispheres dominate the opposite pair.
 1311 Due to the parametric structure of the connectivity matrix, the parameters \mathbf{z} are a linear function
 1312 of the eigenvalues $\boldsymbol{\lambda} = [\lambda_{\text{all}}, \lambda_{\text{side}}, \lambda_{\text{task}}, \lambda_{\text{diag}}]^\top$ associated with these eigenmodes.

$$\mathbf{z} = A\boldsymbol{\lambda} \quad (93)$$

1313

$$A = \frac{1}{4} \begin{bmatrix} 1 & 1 & 1 & 1 \\ 1 & -1 & -1 & 1 \\ 1 & 1 & -1 & -1 \\ 1 & -1 & 1 & -1 \end{bmatrix}. \quad (94)$$

1314 We are interested in the effect of raising or lowering the amplification of each eigenmode in the
 1315 connectivity matrix. To test this, we calculate the unit vector of changes in the connectivity \mathbf{z} that
 1316 result from a change in the associated eigenvalues

$$\mathbf{v}_a = \frac{\frac{\partial \mathbf{z}}{\partial \lambda_a}}{\|\frac{\partial \mathbf{z}}{\partial \lambda_a}\|_2}, \quad (95)$$

1317 where

$$\frac{\partial \mathbf{z}}{\partial \lambda_a} = A \mathbf{e}_a, \quad (96)$$

1318 and e.g. $\mathbf{e}_{\text{all}} = [1, 0, 0, 0]^\top$. So \mathbf{v}_a is the normalized column of A corresponding to eigenmode a .

1319 While perturbations in the sensitivity dimension $\mathbf{v}_1(\mathbf{z}^*)$ adapt with the mode \mathbf{z}^* chosen, perturba-

1320 tions in \mathbf{v}_a for $a \in \{\text{all}, \text{side}, \text{text}, \text{diag}\}$ are invariant to \mathbf{z} (Equation 96).

1321 We tested whether the inferred SC model connectivities could reproduce experimental effects of

1322 optogenetic inactivation in rats [76]. During periods of simulated optogenetic inactivation, activity

1323 was decreased proportional to the optogenetic strength γ

$$x_\alpha = (1 - \gamma)\phi(u_\alpha). \quad (97)$$

1324 Delay period inactivation was from $0.8 < t < 1.2$, choice period inactivation was for $t > 1.2$ and

1325 total inactivation was for the entire trial.